

โครงสร้างโมเลกุลและโครงสร้างอิเล็กทรอนิกส์ของท่อนาโนคาร์บอนผนังเดี่ยวที่เสียรูปและการดูดซับ
ของโลหะแบบประจุสองบวกบนแผ่นกราฟีนออกไซด์



วิทยานิพนธ์นี้เป็นส่วนหนึ่งของการศึกษาตามหลักสูตรปริญญาวิทยาศาสตรดุษฎีบัณฑิต
สาขาวิชาเคมี ภาควิชาเคมี

คณะวิทยาศาสตร์ จุฬาลงกรณ์มหาวิทยาลัย
บทคัดย่อและแฟ้มข้อมูลฉบับเต็มของวิทยานิพนธ์ตั้งแต่ปีการศึกษา 2554 ที่ให้บริการในคลังปัญญาจุฬาฯ (CUIR)
ปีการศึกษา 2556
เป็นแฟ้มข้อมูลของนิสิตเจ้าของวิทยานิพนธ์ ที่ส่งผ่านทางบัณฑิตวิทยาลัย
ลิขสิทธิ์ของจุฬาลงกรณ์มหาวิทยาลัย

The abstract and full text of theses from the academic year 2011 in Chulalongkorn University Intellectual Repository (CUIR)
are the thesis authors' files submitted through the University Graduate School.

MOLECULAR AND ELECTRONIC STRUCTURES OF DEFORMED SINGLE-WALLED
CARBON NANOTUBES AND THE ADSORPTION OF DIVALENT METAL IONS ON
GRAPHENE OXIDE SHEET

Mr. Somphob Thompho



จุฬาลงกรณ์มหาวิทยาลัย
CHULALONGKORN UNIVERSITY

A Dissertation Submitted in Partial Fulfillment of the Requirements
for the Degree of Doctor of Philosophy Program in Chemistry

Department of Chemistry

Faculty of Science

Chulalongkorn University

Academic Year 2013

Copyright of Chulalongkorn University

สมภาพ ฌมโพธิ์ : โครงสร้างโมเลกุลและโครงสร้างอิเล็กทรอนิกส์ของท่อนาโนคาร์บอนผนังเดียวที่เสียรูปและการดูดซับของโลหะแบบประจุสองบวกบนแผ่นกราฟีนออกไซด์. (MOLECULAR AND ELECTRONIC STRUCTURES OF DEFORMED SINGLE-WALLED CARBON NANOTUBES AND THE ADSORPTION OF DIVALENT METAL IONS ON GRAPHENE OXIDE SHEET) อ.ที่ปรึกษาวิทยานิพนธ์หลัก: ศ. ดร.สุพจน์ หารหนองบัว, อ.ที่ปรึกษาวิทยานิพนธ์ร่วม: ดร.อรพรรณ แสงสว่าง, ดร.ธัญญา รุ่งโรจน์ มงคล, 79 หน้า.

ในงานวิจัยนี้มีการศึกษาแผ่นกราฟีนสองชนิด คือท่อนาโนคาร์บอนผนังเดียวและแผ่นกราฟีนออกไซด์ ในการศึกษาสมบัติเชิงโครงสร้างและอิเล็กทรอนิกส์ของท่อนาโนคาร์บอนผนังเดียวที่ความดันสูง มีวัตถุประสงค์เพื่อศึกษาสมบัติของแถบช่องว่างพลังงานที่เกี่ยวข้องกับโครงสร้างของท่อนาโนคาร์บอนแบบอาร์มแชร์และแบบซิกแซกที่มีขนาดและรูปร่างต่าง ๆ ซึ่งดัดแปลงโดยใช้แรงด้วยวิธีการคำนวณทางควอนตัม โดยปรับสัดส่วนของขนาดเส้นผ่าศูนย์กลางด้านยาวต่อด้านสั้นของท่อนาโนคาร์บอนผนังเดียว (*eta*) จากการศึกษาพบว่า เมื่อเพิ่มสัดส่วนของขนาดเส้นผ่าศูนย์กลางด้านยาวต่อด้านสั้นของท่อนาโนคาร์บอนผนังเดียว ความยาวพันธะที่บริเวณด้านบนของท่อใกล้จุดแรงบีบมีค่าเพิ่มขึ้น ขณะที่ความยาวพันธะบริเวณกลางท่อมักมีค่าน้อยลง ส่งผลให้เกิดการเปลี่ยนแปลงค่าการนำไฟฟ้าจากโลหะเป็นสารกึ่งตัวนำของท่อนาโนคาร์บอนผนังเดียวแบบอาร์มแชร์ ขณะที่เกิดการเปลี่ยนแปลงค่าการนำไฟฟ้าจากสารกึ่งตัวนำเป็นโลหะในท่อนาโนคาร์บอนผนังเดียวแบบซิกแซก จากการศึกษาการทดลองนี้อาจนำไปสู่การออกแบบอุปกรณ์อิเล็กทรอนิกส์ในระดับนาโนที่มีประสิทธิภาพมากขึ้น ขณะที่การศึกษาการดูดซับของโลหะหนักแบบประจุสองบวก (Cd^{2+} , Cu^{2+} , Hg^{2+} และ Zn^{2+}) บนแผ่นกราฟีนออกไซด์ที่มีหมู่ฟังก์ชันต่าง ๆ ได้แก่ หมู่ไฮดรอกซิล หมู่เอพอกไซด์ หมู่คาร์บอนิล และหมู่คาร์บอกซิลิก ด้วยทฤษฎีฟังก์ชันความหนาแน่น จากค่าพลังงานของการดูดซับโลหะหนักบนแผ่นกราฟีนออกไซด์สามารถเรียงลำดับประสิทธิภาพการดูดซับได้ดังนี้ $Cu^{2+} > Hg^{2+} > Zn^{2+} > Cd^{2+}$ โดยโลหะหนักมักยึดจับบนตำแหน่งระหว่างหมู่เอพอกไซด์ การเข้าใจถึงพฤติกรรมของโลหะหนักที่เป็นไอออนแบบประจุสองบวกบนพื้นผิวของกราฟีนออกไซด์นี้ สามารถนำไปประยุกต์ใช้ในการกำจัดโลหะหนักของเสียในอุตสาหกรรมต่อไป

ภาควิชา เคมี

สาขาวิชา เคมี

ปีการศึกษา 2556

ลายมือชื่อนิสิต

ลายมือชื่อ อ.ที่ปรึกษาวิทยานิพนธ์หลัก

ลายมือชื่อ อ.ที่ปรึกษาวิทยานิพนธ์ร่วม

ลายมือชื่อ อ.ที่ปรึกษาวิทยานิพนธ์ร่วม

5273903323 : MAJOR CHEMISTRY

KEYWORDS: CARBON NANOTUBE / GRAPHENE OXIDE / DEFORMED / TRANSITION METAL

SOMPHOB THOMPPO: MOLECULAR AND ELECTRONIC STRUCTURES OF DEFORMED SINGLE-WALLED CARBON NANOTUBES AND THE ADSORPTION OF DIVALENT METAL IONS ON GRAPHENE OXIDE SHEET. ADVISOR: PROF. SUPOT HANNONGBUA, Dr.rer.nat., CO-ADVISOR: ORAPHAN SAENGSAWANG, Dr.rer.nat., THANYADA RUNGROTMONGKOL, Ph.D., 79 pp.

The graphene studies are divided into two parts, a single-walled carbon nanotube (SWCNT) and graphene oxide (GO) sheet. Firstly, the molecular and electronic properties of SWCNTs can be modified by deforming their structures under high pressure. The aim of this study was to investigate the energy band gap using quantum calculations, in relation to molecular structures of armchair and zigzag SWCNTs of various sizes and shapes deformed by applied forces. To model an increase in pressure, the degree of flatness (*eta*) of the SWCNTs was adjusted. From obtained results, with increased *eta* values in all studied SWCNTs, the bond lengths at the flattened region were dramatically lengthened, while those at tube edge region were slightly decreased. As a function of the mechanical deformation, an electronic band gap is reduced leading to a change of semiconductor-metallic property for armchair SWCNTs. On the other hand, an electronic band gap is enhanced leading to a change of metallic-semiconductor property of zigzag SWCNTs. These results may contribute to a more refined design of new nano-electronic devices. Secondly, the adsorptions of divalent metal ions (Cd^{2+} , Cu^{2+} , Hg^{2+} and Zn^{2+}) on GO sheet with some functional groups, including hydroxyl, epoxy, carbonyl and carboxyl groups, were studied by density functional theory (DFT). From the binding energies of these divalent metals on the GO surface, the adsorption efficiency of metal ions can be ordered as $\text{Cu}^{2+} > \text{Hg}^{2+} > \text{Zn}^{2+} > \text{Cd}^{2+}$. Moreover, we found that the divalent metal ions likely interacted between the two epoxy groups. Understanding the behavior by which divalent metal ions adsorb on the GO surface it would be useful to design effective controls of the heavy metal pollution in industrial waste.

Department: Chemistry

Student's Signature

Field of Study: Chemistry

Advisor's Signature

Academic Year: 2013

Co-Advisor's Signature

Co-Advisor's Signature

ACKNOWLEDGEMENTS

In the completion of my Doctor Dissertation, I am deeply appreciating to my advisor, Prof.Dr. Supot Hannongbua, and co-advisors Dr.Oraphan Saengsawang and Dr.Thanyada Rungrotmongkol, not only for suggestion on my research but also for teaching academic skills. They also actively encouraged me to overcome any difficulty during this dissertation work. Meanwhile, I could not complete this thesis without Dr. rer. nat. habil. Siegfried Fritzsche, who gives me an inspiration and persuasive instruction.

Next, I would like to thank financial support from The 90th Anniversary of Chulalongkorn University Fund (Ratchadaphiseksomphot Endowment Fund) and a scholarship from the Commission of Higher Education for the Sandwich Ph.D. Program (CHE-PHD-SW). The Computational Chemistry Unit Cell (CCUC) at the Department of Chemistry, Faculty of Science, Chulalongkorn University is acknowledged for computer resources and other facilities. I also thank to CCUC colleagues for helpful and friendship.

I am mostly grateful to my family which is the most important thing in my life. Their unconditional loves have brought me up. I really owe what I am to them; especially, my mother and my father who make me believe in my own way and let grow up as a quality man. My younger sister who looks at me as a role model also intensifies my effort in this graduation.

CONTENTS

	Page
THAI ABSTRACT	iv
ENGLISH ABSTRACT	v
ACKNOWLEDGEMENTS	vi
CONTENTS	vii
LIST OF TABLE	x
LIST OF FIGURE	xi
CHAPTER I	1
INTRODUCTION	1
1.1 Research rationale	1
1.2 Hybridization of carbon	1
1.3 Carbon nanotube	2
1.4 Graphene	7
1.5 Graphene oxide	8
1.6 Objectives of the present study	10
CHAPTER II	11
THEORY	11
2.1 Quantum mechanics	11
2.1.1 History	11
2.1.2 Schrödinger equation in a periodic potential	13
2.1.3 The electronic hamiltonian for the system	15
2.1.4 Bloch's theorem	15
2.2 Approximate methods in quantum mechanics	16
2.2.1 Perturbation theory	16
2.2.2 Hartree-Fock approximation	19
2.2.3 Density functional theory	19
2.2.4 Hybrid functional (B3LYP)	24
2.2.5 Hybrid meta functional (M06)	25

	Page
2.3 Basis set	26
2.3.1 Slater type atomic orbitals	26
2.3.2 Gaussian type atomic orbitals	27
2.3.2 Effective core potential	27
2.4 Plane wave pseudopotential approach	28
2.4.1 Plane wave basis set	29
2.4.2 Reciprocal space	29
2.4.3 Periodicity and special points	30
CHAPTER III	31
METHODOLOGY	31
3.1 Constrained geometry optimization of SWCNTs	31
3.2 Geometrical structures of the zigzag and the armchair SWCNTs	33
3.3 Deformed structures of the SWCNTs	34
3.4 Ab initio pseudopotentials method	34
3.5 Model of the graphene oxide and optimization	34
3.6 Binding energy calculations of GO complexes	37
CHAPTER IV	39
RESULTS AND DISCUSSION	39
4.1 Single-walled carbon nanotubes (SWCNTs)	39
4.1.1 Validation of density functional theory (DFT) methods for SWCNTs	39
4.1.2 Effect of applied force on bond lengths of SWCNTs	40
4.1.3 Effect of applied force on bond angle of SWCNTs	44
4.1.4 Effect of applied force on electronic properties of SWCNTs	45
4.2 The divalent metal cations adsorption on graphene oxide	50
4.2.1 Validation of calculation method for metal-GO complexes binding energies	50
4.2.2 Binding energies of the divalent metal cations on GO sheet	50

	Page
4.2.3 Structural properties of divalent metal cations on GO sheet.....	55
4.2.4 Investigation the behavior of the divalent metal cations on the graphene oxide.....	60
4.2.5 Effect of metal cation with curvature of GO complex	63
4.2.6 Adsorption of Cu^{2+} cation on GO sheet.....	66
CHAPTER V	67
CONCLUSION	67
REFERENCES	70
VITA.....	79

LIST OF TABLE

	Page
TABLE 1. 1: AN OVERVIEW OF VARIOUS PROPERTIES OF CNTS	3
TABLE 3. 1: THE TUBE DIAMETERS OF NATIVE AND DEFORMED SWCNTS AND BOX PARAMETER (Γ)....	33
TABLE 4. 1: METHOD VALIDATION COMPARED BETWEEN CALCULATED AND EXPERIMENTAL VALUES FOR ZIGZAG AND ARMCHAIR OF NORMAL SWCNTS IN TERMS OF BAND GAP (eV).....	39
TABLE 4. 2: ENERGY BAND GAP (eV) FOR NORMAL AND DEFORMED ZIGZAG AND ARMCHAIR SWCNTS WITH FIVE DIFFERENT H VALUES.	47
TABLE 4. 3: BINDING ENERGIES (ΔE_{BIND}), DERIVED ACCORDING TO EQ.3.1, FOR THE BENZENE-CATION (CD^+ , CU^+ , HG^+ , ZN^+ AND AG^+) OBTAINED FROM THIS WORK AND THE PREVIOUS STUDIES. THE DISTANCE (R) WAS MEASURED FROM THE CENTER OF MASS OR THE NEAREST ATOM OF THE BENZENE RING TO THE METAL CATION.	58
TABLE 4. 4: SUMMARY OF CALCULATED RESULTS FOR DIVALENT METAL ADSORPTION ON GRAPHENE OXIDE: THE DISTANCE (D), THE CURVATURE DISTANCES (H) (IN TERMS OF THE SHORTEST DISTANCE BETWEEN THE METAL ATOM AND THE GO PLANE) [\AA] AND BINDING ENERGY; ΔE_{BIND} ($\text{KCAL}\cdot\text{MOL}^{-1}$) OF THE DIVALENT METAL ADSORPTION ON GO SURFACE WITH AND WITHOUT BSSE CORRECTIONS BY USING 6-31G(D) BASIS SET. THE VALUES IN PARENTHESES ARE THE BINDING ENERGIES WITH BSSE CORRECTION. THE VALUE IN BRACKET UNDER METAL ION IS AN IONIC RADIUS (\AA). THE BOND DISTANCES (R_{O1-O3}) WERE MEASURED FROM PROJECTION POINT TO THE OXYGEN ATOM OF FUNCTIONAL GROUPS [\AA]. THE BOND DISTANCE (L_{O1-O3} , L_{O1-O2} AND L_{O2-O3}) WAS MEASURED FROM AN OXYGEN ATOM TO ANOTHER OXYGEN ATOM OF FUNCTIONAL GROUPS [\AA], AND THE ANGLE (θ) IN TERM OF THE ANGLE BETWEEN THE $O_1-O_2-O_3$ PLANE AND THE GO PLANE [DEGREE]	58
TABLE 4. 6: BINDING DISTANCE, R (\AA) AND ANGLES (β) AND (ϕ) BETWEEN THE DIVALENT METAL CATION AND GO SURFACE	56

LIST OF FIGURE

	Page
FIGURE 1. 1: THE BONDING AND ANTI-BONDING ORBITALS IN TERM OF THE THREE SP ² HYBRIDIZATION ..	2
FIGURE 1. 2: SCHEMATIC VIEWS FOR SWCNTs WITH ARMCHAIR ZIGZAG AND CHIRAL STRUCTURES.....	4
FIGURE 1. 3: STRUCTURE OF GRAPHENE IN RECIPROCAL SPACE	8
FIGURE 1. 4: SCHEMATIC DIAGRAM TO PRODUCE GO BY HUMMERS METHOD [41].....	9
FIGURE 1. 5: UV-VIS ABSORPTION SPECTRA OF FREE GO ARE SHOWS A BAND OF TRANSITION.....	9
FIGURE 1. 6: TRANSMISSION INFRARED-ABSORBANCE SPECTRUM OF GO	10
FIGURE 2. 1: SCHEMATIC REPRESENTATION OF THE CUTOFF ENERGY CONCEPT.....	29
FIGURE 3. 1: (A) THE DEGREE OF FLATNESS IS CALCULATED AS $\eta = (D_0 - D)/D_0$. D AND D ₀ ARE THE DIAMETERS SHOWN IN THE FIGURE (B, C) REPRESENTATIVE SWCNTs, Z(10,0) AND A(6,6), WITH TWO DIFFERENT BOND LENGTHS (B _{Z,A} B _{Z,P} AND B _{A,A} B _{A,E}) AND A BOND ANGLE (A) IN A QUADRANT OF THE TUBE COLORED IN ORANGE. 1-5B _{Z,A} , 1-3B _{Z,P} AND A1-A5 WERE DETERMINED FOR Z(10,0) AND 1-4B _{A,E} , 1-3B _{A,A} AND A1-A6 FOR A(6,6).....	32
FIGURE 3. 2: (A) TOP AND (B) SIDE VIEWS OF SCHEMATIC REPRESENTATION OF GRAPHENE OXIDE MODEL	35
FIGURE 3. 3: (A) THE FOUR ADSORPTION SITES, 1-4, OF GO SURFACE FOR EACH ION (B) TOP VIEW OF GO SURFACE WHERE 1 IS THE ION POSITION AT THE CENTER OF GO, 2 IS THE POSITION BETWEEN THE EPOXIDE AND HYDROXYL GROUP AND 3 IS THE POSITION AT THE CENTER OF TWO EPOXIDE GROUPS. (C) BOTTOM-UP VIEW OF GO SURFACE WHERE 4 IS THE ION POSITION BETWEEN THE EPOXIDE AND HYDROXYL GROUP. NOTE THAT THE METAL ION IS PLACED ABOVE THE SURFACE BY 5 Å ON EACH SIDE.	36
FIGURE 4. 1: VARIATION OF C-C BOND LENGTHS, B _{Z,A} AND B _{Z,P} (DEFINED IN FIGURE 3.1B) FOR ZIGZAG (10,0), (15,0), (20,0), (25,0) AND (30,0) SWCNTs, AND B _{A,A} AND B _{A,E} (DEFINED IN FIGURE 3.1C) FOR ARMCHAIR (6,6), (8,8), (10,10), (14,14) AND (17,17)SWCNTs AS A FUNCTION OF FLATNESS (η)	43
FIGURE 4. 2: VARIATION OF C-C-C BOND ANGLES, A (DEFINED IN FIGURE 3.1B) FOR ZIGZAG (10,0), (15,0), (20,0), (25,0) AND (30,0) SWCNTs, AND FOR ARMCHAIR (6,6), (8,8), (10,10), (14,14) AND (17,17) SWCNTs AS A FUNCTION OF FLATNESS (η).....	46

LIST OF FIGURE

	Page
FIGURE 4. 3: ENERGY BAND GAP (eV) OF THE ZIGZAG (10,0), (15,0), (20,0), (25,0) AND (30,0) SWCNTs AS A FUNCTION OF FLATNESS (η)	48
FIGURE 4. 4: ENERGY BAND GAPS (eV) OF THE ARMCHAIR (6,6), (8,8), (10,10), (14,14) AND (17,17) SWCNTs AS A FUNCTION OF FLATNESS (η)	49
FIGURE 4. 5: MODEL OF GRAPHENE OXIDE (GO) SHEET USED IN THIS STUDY. PLANE OF THE GO SHEET (GREEN) AND THE FOUR POSITIONS (1-4) FOR METAL ION ADSORPTION.....	51
FIGURE 4. 6: THE BINDING ENERGY (ΔE_{BIND}) OF FOUR DIVALENT METALS WITH 4 POSITIONS AT B3LYP/6-31G(D)/LANL2DZ BASIS SET.....	52
FIGURE 4. 7: THE ANGLE (β) AND DISTANCES (R_1 - R_3) OF DIVALENT METAL CATION ADSORPTION ON FUNCTIONAL GROUPS OF GO SHEET	55
FIGURE 4. 8: DEFINITION OF THE DISTANCE (D) MEASURED FROM THE DIVALENT CATION TO THE O ₁ -O ₂ -O ₃ PLANE	57
FIGURE 4. 9: DEFINITION OF THE ANGLE (θ) BETWEEN THE O ₁ -O ₂ -O ₃ PLANE AND THE GO PLANE.....	57
FIGURE 4. 10: ANGLE (ϕ) MEASURED BETWEEN TWO PLANES.	58
FIGURE 4. 11: THE PROJECTION DISTANCE (D) AND ANGLE (θ) OF M ²⁺ -GO COMPLEXES WITH 3 POSITIONS AT B3LYP/6-31G(D).	58
FIGURE 4. 12: THE ANGLE (ϕ) OF DIVALENT METAL CATIONS ADSORPTION ON PLANE REFERENCE OF FUNCTIONAL GROUPS.....	59
FIGURE 4. 13: (A) THE DISTANCE (R_0), AND (B) O-O DISTANCE (L_{O-O}) OF CATION-GO COMPLEXES WITH THE THREE OF OXYGEN ATOMS, O ₁ -O ₃	60
FIGURE 4. 14: THE DISTANCE (R_{O1}), AND O-O DISTANCE (L_{O1-O2}) OF M ²⁺ -GO COMPLEXES WITH 3 POSITIONS AT B3LYP/6-31G(D).....	61
FIGURE 4. 15: THE DISTANCE (R_{O2}), AND O-O DISTANCE (L_{O2-O3}) OF M ²⁺ -GO COMPLEXES WITH 3 POSITIONS AT B3LYP/6-31G(D).....	61
FIGURE 4. 16: THE DISTANCE (R_{O3}) AND O-O DISTANCE (L_{O1-O3}) OF M ²⁺ -GO COMPLEXES WITH 3 POSITIONS AT B3LYP/6-31G(D).....	61
FIGURE 4. 17: THE PROJECTION OF DIVALENT METAL CATIONS ON XY-PLANE OF GO. DISTANCE OF CATIONS TO XY-PLANE [\AA] WAS SHADED BY COLOUR.....	63

LIST OF FIGURE

	Page
FIGURE 4. 18: THE CURVATURE ($H_{1,2}$) OF GO COMPLEXES	64
FIGURE 4. 19: THE CURVATURE ($\Delta H_{1,2}$) OF GO COMPLEXES FOUR DIVALENT METALS WITH 4 POSITIONS AT B3LYP/6-31G(D).	65
FIGURE 4. 20: (LEFT) X-RAY PHOTOELECTRON SPECTRA (C1S) OF GO AND GO+CU ²⁺ FROM REF [95] AND (RIGHT) THE ANGLE A RELATE TO DIVALENT CATION ADSORPTION	66



CHAPTER I

INTRODUCTION

1.1 Research rationale

The theoretical understanding of graphene, graphene oxide (GO), carbon nanotubes (CNT) and other carbon based nanomaterials were ambiguous. This study includes understanding the fundamental properties of carbon nanomaterials, the influence of defects on properties, and exploring possibilities for nanoscale carbon electronics and applications. There were two purposes of this research: investigation on the influence of the applied force on the structural and electronic properties of single-walled carbon nanotubes (SWCNTs), and divalent metal cations adsorption on the GO surface. It is expected that the deformed SWCNTs would change their electronic properties, in comparison to the normal SWCNTs while the functional groups on the surface of GO have direct influence on the adsorption of divalent metal cations on GO surface. These findings can be applied to the development of novel nano-electronic devices and effectively utilized for the treatment of industrial waste, respectively.

1.2 Hybridization of carbon

Carbon is the group 4A elements of the periodic table. The four valence electrons were $2s^2$ and $2p^2$ atomic orbital of carbon atom. The hybridization state can be three states such as in sp (e.g. C_2H_2), sp^2 (e.g. graphite) or sp^3 (e.g. CH_4) forms. This property is unique to carbon in its particular group in periodic table. Discoveries and inventions of the size sp^2 carbon bonded materials such as fullerenes, carbon nanotubes and graphene have been investigated in this field. As shown in Figure 1.1, mixing the $2s$ orbital with two $2p$ orbitals called sp^2 hybridization generates these three

orbitals. The π and π^* denotes the bonding and anti-bonding orbital in term of the three sp^2 hybridized orbital are in-plane, with 2p orbital orthogonal to the plane.

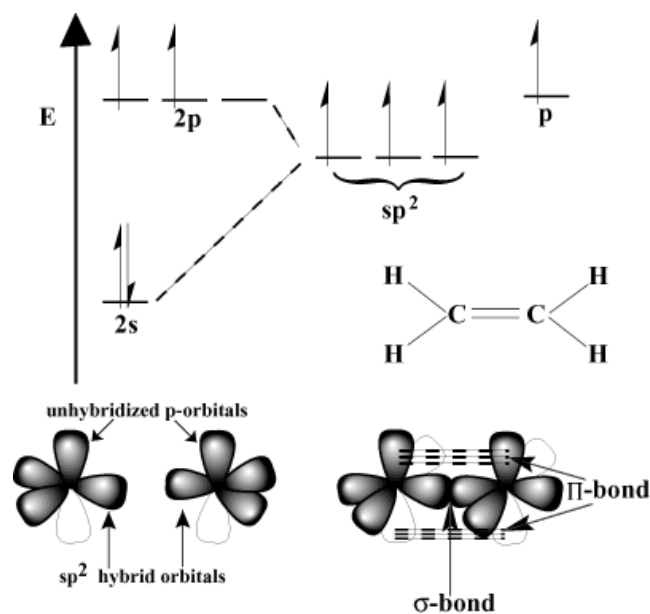


Figure 1. 1: The bonding and anti-bonding orbitals in term of the three sp^2 hybridization

1.3 Carbon nanotube

The carbon nanotube (CNT) has gained much interest in the field of nano-devices because of its very special properties, such as elasticity, strength, flexibility, and conductivity. Table 1.1 gives a summary of experimentally measured properties of CNTs. Their structures are allotropes of carbon in the form of rolled-up graphene sheets [1]. CNTs generally have various structures of the chiral type, have a number of layers, and can be characterized as single-walled carbon nanotubes (SWCNTs), double-walled carbon nanotubes (DWCNTs) or multi-walled carbon nanotubes (MWCNTs) [2]. Many studies in the recent years have focused on the electronic properties of the

carbon nanotubes (CNTs) in order to achieve the desired properties of the nano-devices [2-9].

Table 1. 1: An overview of various properties of CNTs

property	value	unit	reference
carbon bond length	≈ 1.42	Å	[10]
C–C tight binding overlap energy	2.7	eV	[10]
maximum current density	> 0.1	300–1800	[11]
thermal conductivity	1000–6000	kWK^{-1}	[12]
Young's modulus	≈ 300 –1800	GPa	[13]
breaking strength	≈ 30	GPa	[13]

The SWCNTs consisting of a single layer of graphene are favorable for this study due to their simplicity. Although various subtypes of SWCNTs are formed from the same graphite sheet, their electronic properties differ depending on their structures, acting as either metal or semiconductor. Hence, their electronic and related properties of SWCNTs are directly determined by their molecular geometries.

Different types of SWCNTs can be geometrically described by the chiral vector (n,m) where n and m are integers (in Figure 1.2). The chiral vector determines how a graphene sheet is rolled which result in various forms of the tubes [1, 2]. Yet, due to symmetry, the rolled-up graphene sheet may lie between the two extreme forms, the armchair form and the zigzag form. In case of the armchair form (n,n) , the SWCNTs are always metallic while in case of the zigzag $(n,0)$ form, the SWCNTs are metallic only when n is a multiple of 3 and are semi-conductive otherwise [2]. Since the stability and the precision of nano-devices apparently depend on the electronic properties of

the SWCNTs, many attempts have been made in order to achieve the desired electronic properties by altering the geometry of the nanotubes. In the past, experimental and theoretical works had not studied the behavior of the molecular properties of SWCNTs. Therefore, the molecular structure of SWCNTs in the distorted states is unknown.

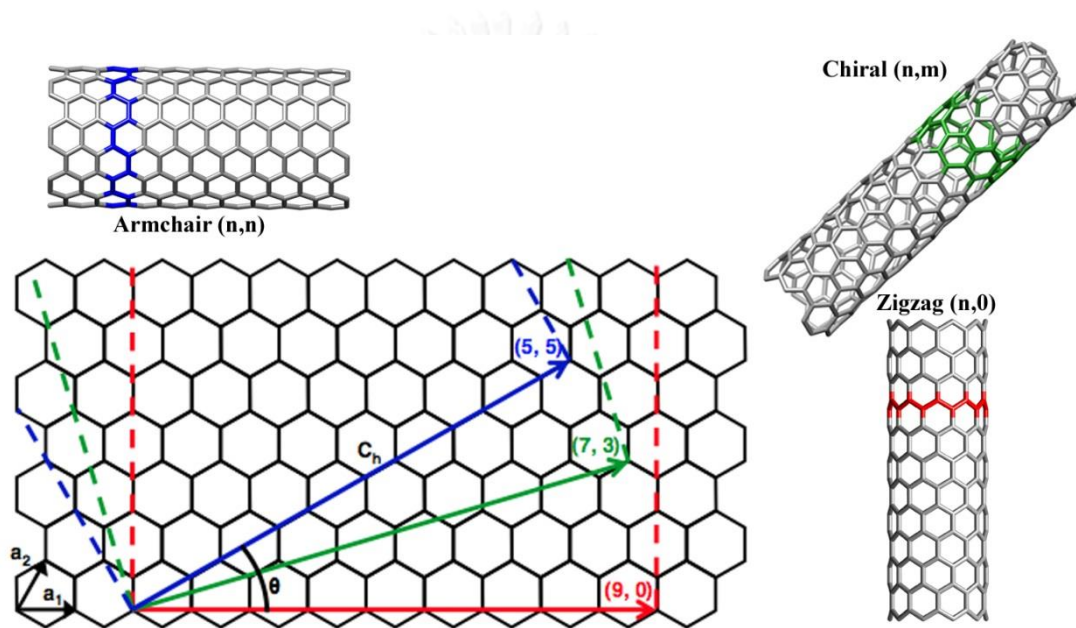


Figure 1. 2: Schematic views for SWCNTs with armchair zigzag and chiral structures

Recently, only the basic molecular properties of deformed SWCNTs have been investigated [14-18]. For example, Gülseren *et al.* [19] showed that the bond lengths and the bond angles have a monotonic variation as a small tubes only. On the other hand, Imtani *et al.* [14, 20, 21] showed that the bond angles of the zigzag and the armchair tubes under hydrostatic pressure were changed only for tubes small radii, but their work did not show the variations in bond lengths and bond angles in all positions along the circumference.

Many experimental studies have examined the electronic properties of SWCNTs after alteration of the molecular structure using mechanical methods such as atomic

force microscopy (AFM). Qing *et al.* demonstrated that local deformation at a crossed SWCNT junction could introduce a local gate effect under ambient conditions [22]. Other studies have induced radial deformations of bent and crossover forms of CNTs using AFM [23-25]. Based on measuring the electrical conductance, MaEuen *et al.* showed that stretching a nanotube with the tip of the AFM can open an electronic band gap in certain metallic nanotubes and change the band gap in semiconducting nanotubes [6]. This behavior also occurs for SWCNTs under high external hydrostatic pressure [26-28]. AFM is widely used due to its ability to alter a certain location of an atom in a specific manner, but this method does not reveal the amount of pressure exerted on the object. A further drawback of AFM is that it does not give enough detailed information about the electronic behavior of SWCNTs. Unfortunately a drawback of this experimental method, it does not give enough detailed information about the electronic behavior of SWCNTs. In fact, another possible way to alter the molecular properties of SWCNTs is by high pressure processing [29-31]. In addition, the amount of pressure required to deform a SWCNT is suspended on the radius of the tube. In fact, the hydrostatic pressure can change the structure and electronic properties including conductivity of SWCNTs, that is, from being a semiconductor to be a metallic tube, and vice versa [32, 33]. However, experimentations on pressure and conductivity can be very complex and expensive. Therefore, there is a need for a detailed theoretical calculation to accurately investigate the behaviors of the nanotubes.

Another feasible way to modify the electronic properties of SWCNTs is by exerting high pressure. Irreversible changes in the mechanical properties of SWCNTs under high pressure have been reported such as the shortening of the tubes [34].

Besides the local Raman scattering spectrum of CNTs studied the effects of bending curvature on its [17], it was found by Wang *et al.* that the CNTs with a bending radii as large as 1–2 μm produce a measurable shift of the frequencies by state deformation. This result was conjured by Raman spectroscopy, the sp^2 C-C bonds in SWCNTs were shifted to sp^3 C-C bonds under high pressure [35].

A major trend in the investigation of the detailed of structure of deformed SWCNTs is the use of quantum calculations, which are able to focus specifically on the electrons and approximations derived from the postulates of quantum mechanics. Most importantly, the theories are able to model the electron behaviors and predict the electronic properties of SWCNTs. Also, there are several theoretical studies based on the first-principle calculation. Avramov *et al.* studied the electronic structures of various types of SWCNTs using PBE and hybrid PBE0 calculations [36] and predicted the density of states (DOS) for metallic and semiconducting tubes, respectively. They found that the PBE energy band gap of the zigzag (10,0) tube is of 0.8 eV in good agreement with the experimental energy band gap of 1.1 eV. Furthermore, the density functional theory within the generalized gradient approximation (GGA) [37] and local density approximation (LDA) with plane wave pseudopotential method [38] suggested that the band gap of this (10,0) tube was reduced from 0.92 eV to 0.00 eV by increasing of the distortion. From the presented evidence, the quantum calculation is a promising theoretical method worthy of a detailed investigation, which is the main objective of this research work.

However, from the previous studies, the structural behavior in terms of the bond lengths and bond angles for deformed SWCNTs as a function of radial deformation have not been revealed in details. For example, the relationship between

the bond lengths and the bond angles under the distorted state. A rational goal of the present work is to investigate the molecular and electronic properties of deformed zigzag and armchair SWCNTs with a variety of tube sizes. To the best of our knowledge this represents the first study in which the impacts of the molecular and electronic properties change of both SWCNTs in detail by quantum calculation.

1.4 Graphene

One has probably made some graphene by drawn a line with a pencil if one as heap up layers of graphene form from graphite pencil sketching. This method can get a graphene sheet with a low-cost and simple way. Graphene is a carbon based material that can be viewed as a one atom thick sheet of graphite. The crystalline allotrope of carbon in a 2-dimensional is graphene. In graphene, carbon atoms are form sp^2 -bonded. Graphene can be described as a single sheet of graphite infinite alternant (only six-member carbon ring) polycyclic aromatic hydrocarbon (PAH). Since graphene has unique properties because of high surface area, high inherent strength and high electrical conductivity [39] (as well as many others). The fundamental properties of graphene have been firstly studied by Novoselov and Geim [40].

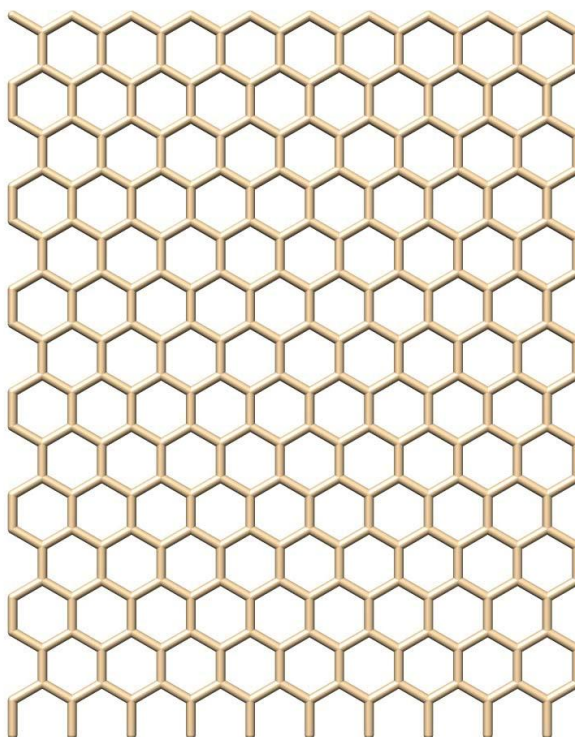


Figure 1. 3: Structure of graphene in reciprocal space

1.5 Graphene oxide

Graphene oxide (GO) is the derivative of graphene, which contains a range of oxygen function group, suchs as epoxy, hydroxyl, and carboxyl groups, on the surface and edge. GO has a hydrophilic functional groups much more than the graphene. Due to, GO have a lone pair electron with the oxygen atom. In the environment field, graphene oxides have been used in nano technology for the waste treatment in industries. Therefore, graphene oxide can be reduced heavy metals ion pollution from an aqueous solution by adsorption on the surface. In this study, adsorption behaviors of heavy metals are not understood. Graphene oxide is produced according to the Hummers method [41] as shown in Figure 1.4. The GO provides an alternative path to single sheets of graphene by chemical reduction of GO.

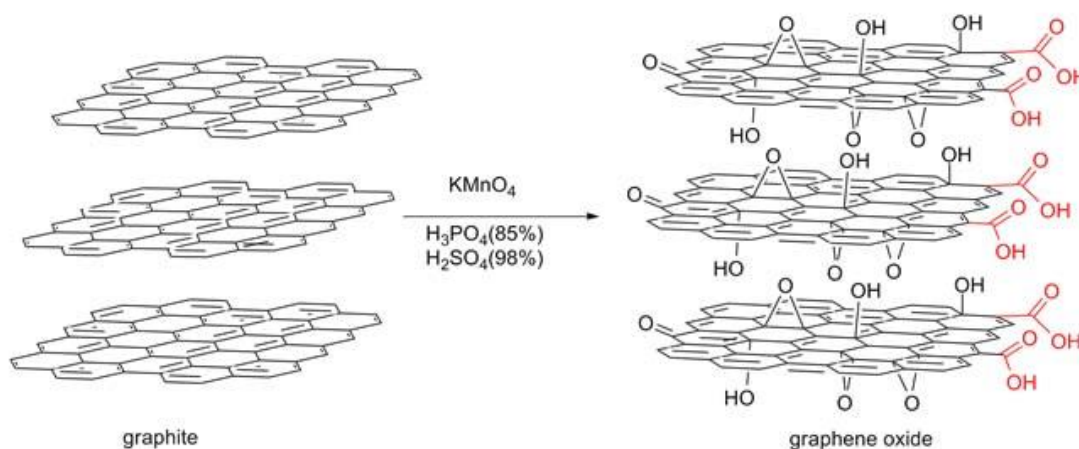


Figure 1. 4: Schematic diagram to produce GO by Hummers method [41]

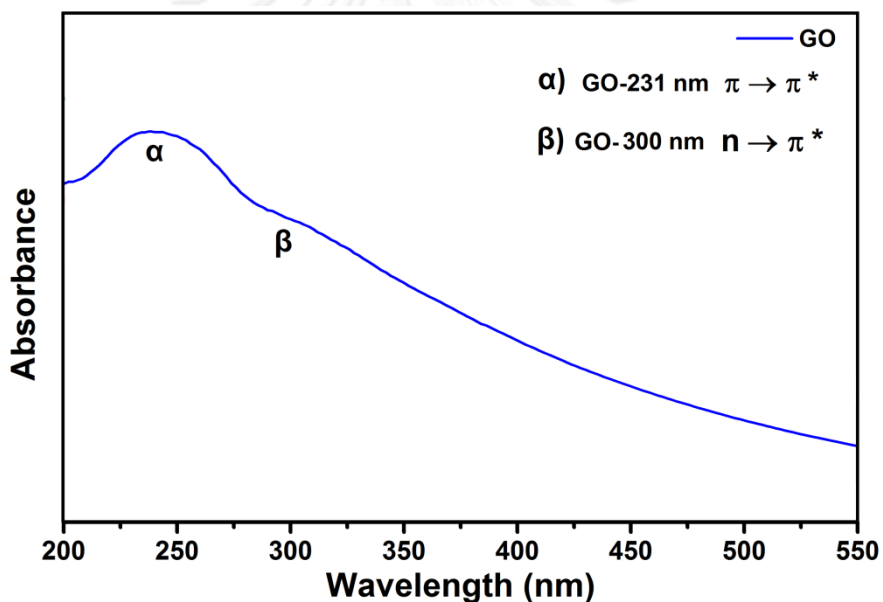


Figure 1. 5: UV-Vis absorption spectra of free GO are shows a band of transition

Figure 1.5 illustrates the absorption spectra of GO. The maximum absorption peak at 231 nm suggested the GO dispersion, which shows the aromatic $\text{C} = \text{C}$ ($\pi - \pi^*$ transition) and $\text{C} = \text{O}$ ($\pi - \pi$ transition) with a band around ~ 300 nm [42]. The graphene oxide structure based on the Lerf-Klinowski model can be confirmed by the experimental structure [43]. The combination of the experiment and the first-principle calculations reveals that an oxygen configuration such as epoxide, hydroxyl, carboxyl

and carbonyl groups. Therefore, the GO model was investigated by some methods to classify functional groups on GO sheet. The possible functional groups on GO surface from infrared spectrum are summarized in Figure 1.6 [43].

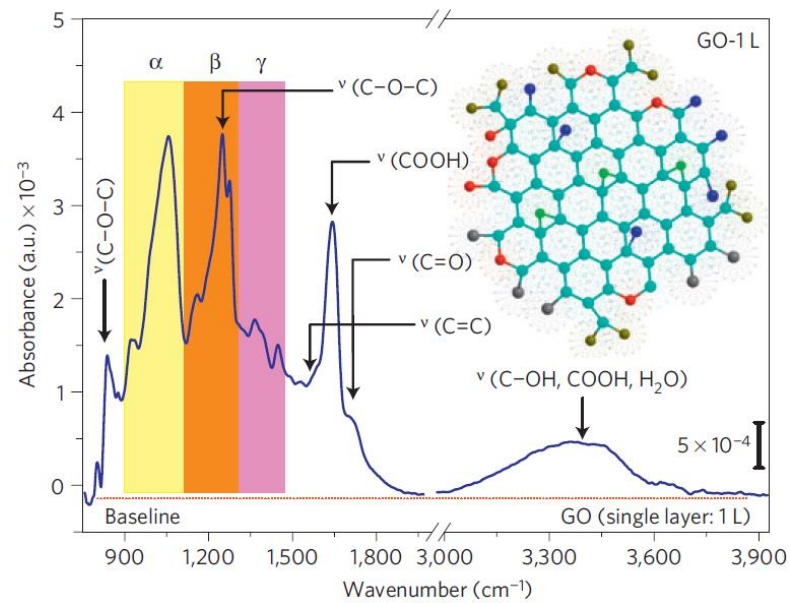


Figure 1. 6: Transmission infrared-absorbance spectrum of GO

1.6 Objectives of the present study

The purpose of this study is to understand (i) the uniqueness of electronic and mechanical properties of various SWCNT forms and (ii) the adsorption of transition metals cations on the GO sheet by using quantum calculations.

CHAPTER II

THEORY

Computational chemistry is caused by fundamental theories of quantum mechanics and statistical mechanics. That called as a research tool of the future, because it can be used to measure the properties of substances in a way calculated to the level of individual atoms or molecules. This is very important, because some chemical experiments for measure the properties of matter are too complex to be done in a real laboratory. So, quantum chemistry is a new way of developing research including the design and structure prediction of chemical or advanced material. The Schrödinger equation is the quantum chemistry equation for most of the computational chemistry scientists use for instance.

2.1 Quantum mechanics

2.1.1 History

The classical model of Bohr (developed in 1913, see [44]) described atoms like planetary systems as consisting of a core around which the electrons are moving on elliptical trajectories like planets around the sun. But according to classical electrodynamics, each charged particle moving on a curved path should send out electromagnetic waves and the electron should; therefore, lose kinetic energy. Finally, it should fall into the core on a spiral path. Planck has proposed already in 1900 a hypothesis that atoms and molecules can emit light of a given frequency ν only in multiples of $h\nu$, where h is a natural constant [45]. This hypothesis enabled him to derive the law of radiation of black bodies. Einstein used it also to explain the

photoelectric effect, and got the Nobel prize for this explanation of the photoelectric effect. But, the reason for this behavior of atoms and molecules remained still unclear until 1924.

The fact that the electron orbitals are stable caused de Broglie to propose the assumption that small particles have essentially a wave nature, and he proposed to describe the electron orbital as a standing wave [46]. Only paths with lengths that are multiples of the wavelengths allowed establishing a standing wave. Otherwise, the parts of the wave would cancel each other. This can explain why only selected stable states can exist.

Connecting Einstein's formula

$$E = mc^2 \quad (2.1)$$

that gives a relation between energy E , mass m , and the vacuum speed of light c , and Planck's formula

$$E = h\nu \quad (2.2)$$

which relates energy E and frequency ν of radiation. De Broglie proposed a model in which each particle of mass m should be accompanied by a wave that is acting even nonlocal in the space surrounding this particle. He was able to show that Planck's formula (2.2) could be derived as a consequence of his wave theory.

The wavelength should be connected with the momentum p of the particle by de Broglie's relation

$$\lambda = \frac{h}{p} \quad (2.3)$$

The wave nature of matter could be proven experimentally by scattering electrons at a crystal [47]. A diffraction pattern characteristic for waves could be observed. De Broglie's picture was very useful, but still too simple to explain several experimental findings.

Finally, Erwin Schrödinger developed the wave theory [48] that could describe the reality quite accurately. The central equation of his theory is the so called Schrödinger equation that he derived from the classical Hamiltonian replacing the momentum or the site of each particle by corresponding operators. If the momentum is replaced by an operator then the coordinate representation will result.

2.1.2 Schrödinger equation in a periodic potential

The most general form of the Schrödinger equation is

$$H\Psi = i\hbar \frac{\partial\Psi}{\partial t} \quad (2.4)$$

where H is the Hamiltonian operator and Ψ is the wave function of the complete system. For a nonrelativistic stable unperturbed particle with mass m moving under influence of an external potential $V(\vec{r})$ the Schrödinger equation reads in coordinate representation

$$-\frac{\hbar^2}{2m} \nabla^2 \Psi(\vec{r}, t) + V(\vec{r}) \Psi(\vec{r}, t) = i\hbar \frac{\partial\Psi(\vec{r}, t)}{\partial t} \quad (2.5)$$

It describes the time development of the state of this particle. If Ψ is correctly normalized then in coordinate representation $|\Psi(\vec{r}, t)|^2$ is the probability density to find the particle at site \vec{r} at time t .

In momentum representation the Schrödinger equation reads

$$\frac{p^2}{2m}\Phi(\vec{p},t) + (2\pi\hbar)^{-3/2} \int V(\vec{p}-\vec{p}')\Phi(\vec{p}',t) = i\hbar \frac{\partial\Phi(\vec{p},t)}{\partial t} \quad (2.6)$$

The transition between both representations of the same equation can be done by Fourier transforms

$$\Phi(\vec{p},t) = (2\pi\hbar)^{-3/2} \int \Psi(\vec{r},t) \exp\left\{-\frac{i}{\hbar}\vec{p}\cdot\vec{r}\right\} d^3\vec{r} \quad (2.7)$$

$$\Psi(\vec{r},t) = (2\pi\hbar)^{-3/2} \int \Phi(\vec{p},t) \exp\left\{-\frac{i}{\hbar}\vec{p}\cdot\vec{r}\right\} d^3\vec{p} \quad (2.8)$$

$$V(\vec{p},t) = (2\pi\hbar)^{-3/2} \int V(\vec{r},t) \exp\left\{-\frac{i}{\hbar}\vec{p}\cdot\vec{r}\right\} d^3\vec{r} \quad (2.9)$$

$$V(\vec{r},t) = (2\pi\hbar)^{-3/2} \int V(\vec{p},t) \exp\left\{-\frac{i}{\hbar}\vec{p}\cdot\vec{r}\right\} d^3\vec{p} \quad (2.10)$$

In the case of a time independent potential U and time independent borders of the system the separation ansatz

$$\Psi(\vec{r},t) = \Phi(\vec{r}) \exp\left\{-\frac{i}{\hbar}Et\right\} \quad (2.11)$$

can be made where E is the total energy.

This leads to the time independent Schrödinger equation (we use now the common notation with $\Psi(\vec{r})$ throughout which is of course not the same function as $\Psi(\vec{r},t)$, but is rather the Φ in equation (2.11))

$$-\frac{\hbar^2}{2m}\Delta\Psi(\vec{r}) + V(\vec{r})\Psi(\vec{r}) = E\Psi(\vec{r}) \quad (2.12)$$

2.1.3 The electronic hamiltonian for the system

For a fundamental understanding of the interaction of a particle with the electronic field we need to know the total energy of the system consisting of particle and field. The nuclear kinetic energy terms are omitted from the Coulomb Hamiltonian and one considers the remaining Hamiltonian as a Hamiltonian of electrons only. This Hamiltonian has been simplified to the so-called electronic Hamiltonian, which acts only on functions of the electronic coordinates.

$$\hat{H}_{el} = \hat{T}_e + \hat{V}_{ne} + \hat{V}_{ee} \quad (2.13)$$

2.1.4 Bloch's theorem

A theorem relating to the quantum mechanics of crystals stating that the wave function Ψ for an electron in a periodic potential has the form

$$\Psi = \exp(ik \cdot r)u(r) \quad (2.14)$$

where k is the wave vector, r is a position vector, and $U(r)$ is a periodic function that satisfies

$$U(r + R) = u(r) \quad (2.15)$$

for all vectors R of the Bravais lattice of the crystal. Bloch's theorem is interpreted to mean that the wave function for an electron in a periodic potential is a plane wave modulated by a periodic function. This explains why a free-electron model has some success in describing the properties of certain metals although it is inadequate to give a quantitative description of the properties of most metals.

2.2 Approximate methods in quantum mechanics

2.2.1 Perturbation theory

The complete Schrödinger equation can be solved only for few special cases. For molecular systems, the treatment is usually restricted to the time independent case. Hence, the method shall be described here only for the case that the Schrödinger equation reads

$$H|\Psi\rangle = E|\Psi\rangle \quad (2.16)$$

Let $H^{(0)}$ be the unperturbed Hamiltonian for which a complete set of orthonormal eigenfunctions $|\Phi_n^{(0)}\rangle$ is known.

$$H^{(0)}|\Phi_n^{(0)}\rangle = E_n^{(0)}|\Phi_n^{(0)}\rangle \quad \langle\Phi_m^{(0)}|\Phi_n^{(0)}\rangle = \delta_{mn} \quad (2.17)$$

Let $H = H^{(0)} + \varepsilon H^{(1)}$ be the Hamiltonian of the perturbed system. Then, we introduce a formal parameter ε that is essentially equal to one but, will have practical importance as it will be seen.

We write the perturbed Hamiltonian formally as $H^{(0)} + \varepsilon H^{(1)}$. We assume that the eigenfunction for the perturbed n-th state fulfills

$$\left(H^{(0)} + \varepsilon H^{(1)}\right)|\Phi_n\rangle = E_n|\Phi_n\rangle \quad (2.18)$$

We will see that in the ansatz

$$E_n = \sum_{k=0}^{\infty} \varepsilon^k E_n^{(k)} \quad |\Phi_n\rangle = \sum_{k=0}^{\infty} \varepsilon^k |\Phi_n^{(k)}\rangle \quad (2.19)$$

the $|\Phi_n^{(k)}\rangle$ and $E_n^{(k)}$ can be calculated by the so called perturbation theory. For the

$|\Phi_n^{(k)}\rangle$ we set the additional conditions that

$$\langle \Phi_n^{(0)} | \Phi_n^{(k)} \rangle = \delta_{0k} \quad \langle \Phi_n | \Phi_n^{(k)} \rangle = \delta_{0k} \quad (2.20)$$

Inserting ansatz (2.41) into equation (2.39) we get

$$\begin{aligned} & (H^{(0)} + \varepsilon H^{(1)}) \left(|\Phi_n^{(k)}\rangle + \varepsilon |\Phi_n^{(1)}\rangle + \varepsilon^2 |\Phi_n^{(2)}\rangle + \dots \right) \\ &= (E_n^{(0)} + \varepsilon E_n^{(0)} + \varepsilon^2 E_n^{(2)} + \dots) \left(|\Phi_n^{(0)}\rangle + \varepsilon |\Phi_n^{(1)}\rangle + \varepsilon^2 |\Phi_n^{(2)}\rangle + \dots \right) \end{aligned} \quad (2.21)$$

We assume that equal powers of ε on both sides of the resulting equations belong to the same level of approximation. The order zero gives

$$H^{(0)} |\Phi_n^{(0)}\rangle = E_n^{(0)} |\Phi_n^{(0)}\rangle$$

which is equation (2.38).

The first order gives

$$H^{(0)} |\Phi_n^{(0)}\rangle + H^{(1)} |\Phi_n^{(0)}\rangle = E_n^{(0)} |\Phi_n^{(1)}\rangle + E_n^{(1)} |\Phi_n^{(0)}\rangle \quad (2.22)$$

Multiplying from left with $\langle \Phi_n^{(0)} |$ we get for this order with $\langle \Phi_n^{(0)} | \Phi_n^{(0)} \rangle = 1$

$$\langle \Phi_n^{(0)} | H^{(0)} | \Phi_n^{(1)} \rangle + \langle \Phi_n^{(0)} | H^{(1)} | \Phi_n^{(0)} \rangle = E_n^{(0)} \langle \Phi_n^{(0)} | \Phi_n^{(1)} \rangle + E_n^{(1)}$$

Because of $\langle \Phi_n^{(0)} | H^{(0)} = \langle \Phi_n^{(0)} | E_n^{(0)}$ this means

$$E_n^{(0)} \langle \Phi_n^{(0)} | \Phi_n^{(1)} \rangle + \langle \Phi_n^{(0)} | H^{(1)} | \Phi_n^{(0)} \rangle = E_n^{(0)} \langle \Phi_n^{(0)} | \Phi_n^{(1)} \rangle + E_n^{(1)}$$

The first order gives therefore

$$\langle \Phi_n^{(0)} | H^{(1)} | \Phi_n^{(0)} \rangle = \langle \Phi_n^{(0)} | E_n^{(1)} | \Phi_n^{(0)} \rangle = E_n^{(1)}$$

That means, we can calculate $E_n^{(1)}$ from

$$E_n^{(1)} = \langle \Phi_n^{(0)} | H^{(1)} | \Phi_n^{(0)} \rangle \quad (2.44)$$

Because the $|\Phi_n^{(0)}\rangle$ form a complete set, we can develop $|\Phi_n^{(k)}\rangle$ as

$$|\Phi_n^{(k)}\rangle = \sum_{l=0, l \neq n}^{\infty} c_{n,l}^{(k)} |\Phi_l^{(0)}\rangle \quad (2.45)$$

Inserting this with $k = 1$ in equation (2.42) we find

$$H^{(0)} \sum_{l=0, l \neq n}^{\infty} c_{n,l}^{(1)} |\Phi_l^{(0)}\rangle + H^{(1)} |\Phi_n^{(0)}\rangle = E_n^{(0)} \sum_{l=0, l \neq n}^{\infty} c_{n,l}^{(1)} |\Phi_l^{(0)}\rangle + E_n^{(1)} |\Phi_n^{(0)}\rangle$$

Multiplying from left with $\langle \Phi_m^{(0)} | \neq \langle \Phi_n^{(0)} |$ we get

$$\begin{aligned} & \langle \Phi_m^{(0)} | H^{(0)} \sum_{l=0, l \neq n}^{\infty} c_{n,l}^{(1)} |\Phi_l^{(0)}\rangle + \langle \Phi_m^{(0)} | H^{(1)} |\Phi_n^{(0)}\rangle \\ &= E_n^{(0)} \langle \Phi_m^{(0)} | \sum_{l=0, l \neq n}^{\infty} c_{n,l}^{(1)} |\Phi_l^{(0)}\rangle + \langle \Phi_m^{(0)} | E_n^{(1)} |\Phi_n^{(0)}\rangle \end{aligned}$$

Hence,

$$\sum_{l=0, l \neq n}^{\infty} c_{n,l}^{(1)} E_n^{(0)} \delta_{ml} + \langle \Phi_m^{(0)} | H^{(1)} |\Phi_n^{(0)}\rangle = E_n^{(0)} \sum_{l=0, l \neq n}^{\infty} c_{n,l}^{(1)} \delta_{ml} + 0$$

$$c_{n,m}^{(1)} E_n^{(0)} + \langle \Phi_m^{(0)} | H^{(1)} |\Phi_n^{(0)}\rangle = E_n^{(0)} c_{n,m}^{(1)}$$

So we finally get (using the notation l instead of m again)

$$c_{n,l}^{(1)} = \frac{\langle \Phi_l^{(0)} | H^{(1)} | \Phi_n^{(0)} \rangle}{E_n^{(0)} - E_l^{(0)}} \quad (2.23)$$

These $c_{n,l}^{(1)}$ equation (2.46) yields a first approximation $|\Phi_n^{(1)}\rangle$ for the n -th wave function of the perturbed system as an infinite series.

In the same scheme higher approximations for eigenvalues and wave functions can be obtained. This shows how perturbation theory using a complete set of basic wave functions can in principle solve the perturbed problem. Note however, that it is not at all sure that the series converge and which basic set is the best one. A lot of skill and experience is needed to apply perturbation theory successfully.

2.2.2 Hartree-Fock approximation

If a system of several particles of equal kind (e.g. electrons) is under consideration then the Hartree-Fock approximation allows a relatively simple treatment. For electrons in this approximation an ansatz is used in which the wavefunction of all electrons is represented by a single Slater determinant with one spin orbital per electron. According to the Rayleigh-Ritz principle, the true ground state wave function of a given system yields the lowest expectation value for the energy in comparison to all other wave functions. Hence, among different approximations to the real wave function the one which gives the lowest energy is considered to be the one closest to the real state. This principle is used to find appropriate spin orbitals for the mentioned Slater determinant used in the Hartree-Fock approximation. An disadvantage of the Hartree-Fock approximation is that electron correlations are partially neglected.

2.2.3 Density functional theory

The density functional theory (DFT) is an approximate method to solve quantum mechanical problems by optimizing an expression called density functional using the Rayleigh-Ritz principle. A functional is a mathematical expression (e.g. an integral) that contains functions. The value of the functional depends upon the whole

functions for all values of their arguments. In the case of the DFT such functions that enter the functional are electron density distributions.

Recently, the DFT has been improved a lot and is now among the most popular methods in quantum physics and chemistry. The electron density, $\rho(\mathbf{r})$, represents the probability of observing an electron at the point \mathbf{r} so that the electron density is manifestly nonnegative, and hence is a physical observable.

The electronic Hamiltonian can be written to accommodate generalization as

$$\hat{H} = \hat{T} + \hat{V}_{ee} + \sum_{i=1}^N v(\mathbf{r}_i) \quad (2.24)$$

where \hat{T} is the kinetic energy operator, \hat{V}_{ee} is the electron-electron interaction energy operator, and the function $v(\mathbf{r})$ is called the electronic external potential which models forces that act on the electrons in the system but are not due to other electrons in the system, as such forces are *external* to the system of electrons. The electronic Hamiltonian in eq. (2.47) is a functional (a function of a function) of the external potential $v(\mathbf{r})$ and a function of the number of electrons (N) and is denoted as $\hat{H}[v(\mathbf{r}); N]$. The external potential is a simple function of the nuclear charges and positions which are determined by locating the cusps of a molecule's ground state electron density. Thus, $v(\mathbf{r})$ is a functional of $\rho(\mathbf{r})$ if and only if no electron density is the ground state density for more than one external potential.

The total electronic energy is also a functional of the external potential and the number of electrons; hence the total energy can be expressed as a functional of the electron density:

$$\begin{aligned}
E[\rho(r)] &\equiv E[v[\rho; r]; N[\rho]] \\
&= \langle \Psi[\rho] | \hat{H}[\rho] | \Psi[\rho] \rangle
\end{aligned}
\tag{2.25}$$

where $\Psi[\rho]$ is the ground state wave function for the Hamiltonian $\hat{H}[\rho]$. Because the external potential is a functional of the electron density, the contribution of the external potential to the total energy can be expressed as

$$V_{ext}[\rho] \equiv \int \rho(r) v[\rho; r] dr \tag{2.26}$$

Thus, the purely electronic contribution to the total energy can be expressed as

$$F[\rho] \equiv E[\rho] - \int \rho(r) v[\rho; r] dr \tag{2.27}$$

$$F[\rho] \equiv \langle \Psi[\rho] | \hat{F} | \Psi[\rho] \rangle \tag{2.28}$$

$F[\rho]$ is called the *Hohenberg-Kohn functional* which is a so-called *universal density functional*. Understanding and computing $F[\rho]$ is almost the whole subject of density functional theory. Hohenberg and Kohn expressed the second theorem which is according to the variational principle as: for the N-electron system with external potential $v[\rho; r]$, the energy of a *N-electron trial density*, $\tilde{\rho}^{(0)}$, is always greater than or equal to the true ground state energy of the system. Moreover, equality is achieved if and only if $\tilde{\rho}^{(0)}$ is the ground state density for this system,

$$E_0 \equiv E_{v_0}[\rho_0] \leq E_{v_0}[\tilde{\rho}^{(0)}] \tag{2.29}$$

where $\rho_0(r)$ is the exact N-electron ground state density.

A prescription to obtain the energy from the N-electron density was given by Kohn and Sham [49] in an one-electron formalism, where in the auxiliary functions

introduced are spin orbitals, feeling only a local potential $v(\mathbf{r})$ which yields exactly the same density as the system of interacting electrons with potential $v(\mathbf{r})$. The electron density, $\rho(\mathbf{r})$, is represented by the sum of the densities of the $\frac{N}{2}$ doubly occupied single-particle spatial orbitals,

$$\rho(\mathbf{r}) = 2 \sum_{i=1}^{\frac{N}{2}} |\psi_i(\mathbf{r})|^2 \quad (2.30)$$

and the Kohn-Sham expression for the electronic energy functional is given by:

$$E[\rho] = T_s[\rho] + V_N[\rho] + J_{ee}[\rho] + E_{xc}[\rho] \quad (2.31)$$

where $T_s[\rho]$ is the non-interacting kinetic energy, $V_N[\rho]$ describes the electron-nuclei interaction, and $J_{ee}[\rho]$ is the classical electrostatic repulsion energy among the electrons:

$$T_s[\rho] = -\frac{1}{2} \sum_i^N \int \psi_i^*(\mathbf{r}) \nabla^2 \psi_i(\mathbf{r}) d\mathbf{r} \quad (2.32)$$

$$V_N[\rho] = \int \rho(\mathbf{r}) v(\mathbf{r}) d\mathbf{r} \quad (2.33)$$

$$J_{ee}[\rho] = \frac{1}{2} \iint \frac{\rho(\mathbf{r}) \rho(\mathbf{r}')}{|\mathbf{r} - \mathbf{r}'|} d\mathbf{r} d\mathbf{r}' \quad (2.34)$$

The last term in eq. (2.57), $E_{xc}[\rho]$, is the exchange-correlation energy functional, which has to correct the electron-electron repulsion, $V_{ee}[\rho]$, being described only by the Coulombic repulsion, $J_{ee}[\rho]$, thereby neglecting the exchange interaction and the electron correlation interaction and for the kinetic energy functional which describes the kinetic energy for non-interacting electrons:

$$E_{xc} = V_{ee}[\rho] - J_{ee}[\rho] + T[\rho] - T_s[\rho] \quad (2.35)$$

Furthermore, the exchange-correlation energy functional should also correct a spurious self-interaction arising from J_{ee} , which is cancelled exactly by the exchange term in *ab initio* methods, but in DFT actually is the largest contribution to E_{xc} .

The electronic ground state density is found by minimizing the Kohn-Sham energy functional, which is achieved by solving the Kohn-Sham equations:

$$\hat{H}^{KS} \psi_i = \left[-\frac{\nabla^2}{2} + v(r) + \frac{1}{2} \int \frac{\rho(r')}{|r-r'|} dr + \frac{\delta E_{xc}[\rho]}{\delta \rho(r)} \right] \psi_i = \epsilon_i \psi_i \quad (2.36)$$

This **KS** equations are nonlinear partial differential equations, which are generally solved employing a *self-consistent field* scheme. However, an exact expression for $E_{xc}[\rho]$ is to date unknown, and the construction of approximated functional is very complex. Moreover, there is no straightforward way in which the exchange-correlation functional can be systematically improved.

The simplest model system in the context of density functional theory is the uniform electron gas, constant electron density ($\rho(r) = \rho$), which has an infinite number of bound electrons and so the total energy of the system is infinite. It can be written as

$$E_{xc}^{LD} = \int \rho(r) \epsilon_{xc}(\rho(r)) dr \quad (2.37)$$

The exchange-correlation energy density function, $\epsilon_{xc}(\rho(r))$, especially in solid-state physics, LDA works surprisingly well despite its approximate nature. However, most chemical applications do not satisfy the restriction of slowly varying electron density, and hence the LDA fails. To extend the approximation, the gradient of the charge

density, $\nabla\rho(r)$, is included to account for the non-homogeneity of the true electron density. This has led to the development of various so-called generalized gradient approximations (GGA) [50], which depend explicitly on local densities and local spin-density gradients as:

$$E_{xc}^{GGA} = \int f[\rho_\alpha(r), \rho_\beta(r), \nabla\rho_\alpha(r), \nabla\rho_\beta(r)] d^3r \quad (2.38)$$

The most popular GGA exchange functional was developed by Becke [51]:

$$E_{xc}^B = -\beta \sum_\sigma \int \rho_\sigma^{4/3} \frac{x_\sigma^2}{(1 + 6\beta x_\sigma \sinh^{-1} x_\sigma)} d^3r \quad (2.39)$$

where x_σ is a dimensionless nonuniformity parameter defined by

$$x_\sigma = \frac{|\nabla\rho_\sigma|}{\rho_\sigma^{4/3}} \quad (2.40)$$

and β is a constant of value 0.0042 as determined by fit to exact Hartree-Fock exchange energies of the noble gas atoms (He through Rn) [51]. A large number of other GGA functionals for both correlation and exchange have been developed, of which the most popular probably are the 3 parameter Lee-Yang-Parr (LYP) correlation function [52, 53], the Perdew86 correlation functional [54] and the Perdew91 exchange and correlation functional [55]. In this thesis, hybrid functionals which introduce an additional HF terms for the exchange such as B3LYP, B3PW91 and B3PW86 were used for comparison of geometry and binding energy results.

2.2.4 Hybrid functional (B3LYP)

More recently, following an approach proposed by Becke the combination of DFT functionals with ab initio formulations leads to a class of expressions, which are essentially a mixture of both DFT and HF contributions with fitted coefficients for each

contribution. The aim of this approach is to provide expressions that include the full exchange contribution with avoiding side-effects that arise from a complete replacement of the DFT exchange expression by the HF one. As an example, the B3LYP functional look likes this.

$$E_{xc}^{B3LYP} = a_{x0}E_x^S + (1 - a_{x0})E_x^{HF} + a_{x1}\Delta E_X^B + E_C^{VWN} + a_c\Delta E_C^{LYP} \quad (2.41)$$

With parameters $a_{x0} = 0.80$, $a_{x1} = 0.72$ and $a_c = 0.81$. These values were obtained from fitting of a selected set of molecules to reproduce heat of formation. The term E_x^{HF} is calculated using the Kohn-Sham orbitals in the manner of HF procedure by computing the exchange integrals $(\nu\mu|\mu\nu)$, E_x^S is Slater local density exchange, E_x^B is Becke's 1988 [51], the Slater exchange along with correction involving the gradient of the density. E_C^{VWN} is Vosko, Wilk and Nusair [56]. Correlation functional and E_C^{LYP} is the correction function of Lee, Yang and Parr [53].

2.2.5 Hybrid meta functional (M06)

These functionals are based on meta-GGA approximations, developed by a group of Prof. Donald G. Truhlar [57] at the University of Minnesota. The exchange-correlation (XC) functional can make an accuracy of a DFT calculation. Therefore, they have been developed and validation of XC functionals. The timeline of develop process were three generation steps. The first generation of functionals is called the local spin density approximation (LSDA), this functionals consider the up- and down-spin. The second generation is generalized gradient approximation (GGA), it focus on the local spin density and their gradients. In third generation functionals, two additional variables, the spin kinetic energy densities are included in the functional form; we called meta-GGAs. Hybrid functionals are containing HF exchange, and they are more

accurate than local functionals for main-group thermochemistry. The Kohn–Sham orbitals were the accurate if HF exchange would be exact determined. The hybrid exchange–correlation energy can be written as follows:

$$E_{xc}^{hyb} = \frac{X}{100} E_X^{HF} + \left(1 - \frac{X}{100}\right) E_X^{DFT} + E_C^{DFT} \quad (2.42)$$

where E_X^{HF} is the nonlocal Hartree–Fock (HF) exchange energy, X is the percentage of Hartree–Fock exchange in the hybrid functional, E_X^{DFT} is the local DFT exchange energy, and E_C^{DFT} is the local DFT correlation energy.

The development of new functional forms for meta-GGAs and hybrid meta-GGAs and their validation against diverse databases have yielded powerful new density functionals with broad applicability to many areas of chemistry. Therefore, the problems involving rearrangements of both organic and transition metal bonds were used M06.

2.3 Basis set

Most molecular quantum-mechanical methods begin the calculation with the choice of a basis set. It is a set of functions which are combined in linear combinations to create molecular orbitals. The use of an adequate basis set is an essential requirement for success of the calculation. Two types of atomic basis functions have received widespread use, Slater Type Orbitals (STO) and Gaussian Type Orbitals (GTO).

2.3.1 Slater type atomic orbitals

The Slater-type orbitals (STO) is written as

$$\phi = Nr^{n-1} e^{-\zeta r} Y_l^m(\theta, \Theta) \quad (2.43)$$

where r , θ and Θ are spherical coordinate, $Y_l^m(\theta, \Theta)$ is spherical harmonics function (the angular part of the wave function) while N , n and ζ are normalization constant, principle quantum number and orbital exponent respectively. The STO provide reasonable representations of atomic orbitals with standard ζ -values recommended by Slater. They are, however, not well suited to numerical work, and their use in practical molecular orbital calculations has been limited. Their largest problem is that it is prohibitively complicated to calculate the matrix elements entering the Fock matrix.

2.3.2 Gaussian type atomic orbitals

The Gaussian Type Orbitals (GTO) is written as

$$\phi = Nx^a y^b z^c e^{-\zeta r^2} \quad (2.44)$$

Where x , y , and z are Cartesian coordinate and a , b and c are non-negative integers. The GTOs have the important advantage that all integrals in the computations can be evaluated explicitly without recourse to numerical integration.

2.3.2 Effective core potential

DFT pseudopotential for all-electron calculations and construct a numerical, the fhi98PP code was perform by Troullier-Martins [58]. The core and valence regions were a balanced basis requires a proper. For transition metal, there are a lot of core electrons (1st-5th periods). Most of the computational effort was used to describe the

energy but not the valence region. In case of LANL2DZ, core electrons are modeled by suitable potential function, and only the valence are treated explicitly.

2.4 Plane wave pseudopotential approach

In all of the calculations in this work, we use the plane wave pseudopotential approach to solving the Kohn-Sham equations. This involves using a plane wave basis set to represent the orbitals, and pseudopotentials to represent the nuclei and core electrons. In this section, we will describe this plane wave pseudopotential approach. Alternative approaches to the plane wave pseudopotential exist. These involve using basis functions that are localized around individual atoms [59].

One advantage of this method is that it has been shown to have accuracy close to the all-electron method for many applications, and yet is still fast enough to treat hundreds of atoms. The portability and accuracy of this code make it a desirable first-principles simulation tool in the study of complex molecular, liquid, and solid-state systems. Applications for this P3MD code include the calculation of free energies, search for structural minima, and ab-initio QMD simulation of quantum liquids in compressed and expanded systems.

2.4.1 Norm-conserving pseudopotentials

The main requirement of the pseudopotential approach is that it reproduces the valence charge density associated with chemical bonds. It has been shown that for pseudo and all-electron wavefunctions to be identical beyond the core radius, R_c , it is necessary for the integrals of squared amplitudes of the two functions be the same. This is equivalent to requiring norm-conservation from pseudo wavefunctions,

i.e. that each of them should carry exactly one electron. This condition ensures that the scattering properties of the pseudopotential are reproduced correctly.

2.4.1 Plane wave basis set

The plane-wave basis set for the electronic wavefunctions at each k-point were preform by bloch's theorem states. In principle, an infinite number of plane waves is required for such an expansion. However, the coefficients, $C_{\mathbf{k}+\mathbf{G}}$, for the plane waves with small kinetic energies, $|\mathbf{k}+\mathbf{G}|^2$, are more important than those with large kinetic energies. Thus, the plane wave basis set can be truncated to include only plane waves that have kinetic energies that are smaller than some particular cutoff energy as illustrated in Figure 2.1 (the radius of the sphere is proportional to the square root of the cutoff energy).

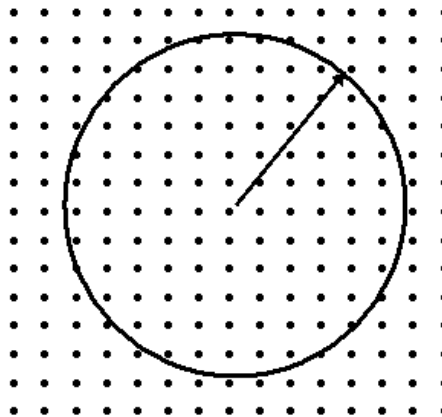


Figure 2. 1: Schematic representation of the cutoff energy concept

2.4.2 Reciprocal space

By analogy with our definition of a one-dimensional Fourier transform, the three dimensional Fourier transforms can be defined as: definition of Fourier transform

$$F(\vec{k}) = \int_{-\infty}^{\infty} f(\vec{r}) e^{-i\vec{k}\cdot\vec{r}} d^3r \quad (2.45)$$

The only differences between this and the one-dimensional equivalent are that F and f are functions of three-dimensional vectors K and r respectively, and the product in the exponential is now a vector dot product.

2.4.3 Periodicity and special points

$$\begin{aligned}\psi_{k+G} &= \exp(i(k+G)\cdot r)u_{k+G}(r) \\ &= \exp(ik\cdot r)u_k(r)\end{aligned}\tag{2.46}$$

where $u_k(r)$ is still periodic in the unit cell, as $\exp(iG\cdot r)$ must be periodic in the unit cell. We can always choose to reduce any k in this fashion, and do always choose to work with $|k| \leq G/2$. This also implies that the points $(\pm \frac{1}{2}, \pm \frac{1}{2}, \pm \frac{1}{2})$ are all identical, for they are related via the addition/subtraction of a reciprocal lattice vector. This point is called the L point, and the reciprocal space point $(0, 0, 0)$ is called the Γ point. A small zoo of other, high-symmetry, points in k -space has also been named.

CHAPTER III

METHODOLOGY

3.1 Constrained geometry optimization of SWCNTs

All system preparations and calculations of zigzag (Z) and armchair (A) SWCNTs with periodic boundary condition were initially generated and optimized using the Cambridge Serial Total Energy Package (CASTEP) module implemented in Material Studio 5.5 (MS) program [60]. *Ab initio* calculations of SWNTs were conducted using various modules available in the commercial software, Materials Studio (Accelrys Inc). Specifically, density functional theory (DFT) calculations were performed with CASTEP modules. Density-functional calculations are performed using plane-wave pseudopotential, which is a method within the generalized gradient approximation (GGA). Ultrasoft pseudopotential is used to model the ion-electron interaction. The cutoff energy for the plane-wave basis is chosen as 300 eV, while further increasing the cutoff shows slightly difference on the results. The present calculations were performed based on the density functional theory (DFT) and within the CASTEP plane wave code [61]. The generalized gradient approximation (GGA) of Perdew–Burke–Ernzerh method parameterized by Perdew, and was used to calculate the exchange and correlation terms. Brillouin-zone integrations were performed using Monkhorst and Pack k-point meshes [62]. During the calculation, the 300 eV for cutoff energies and $6 \times 6 \times 12$ for the numbers of k-point can ensure the convergence for the total energy.

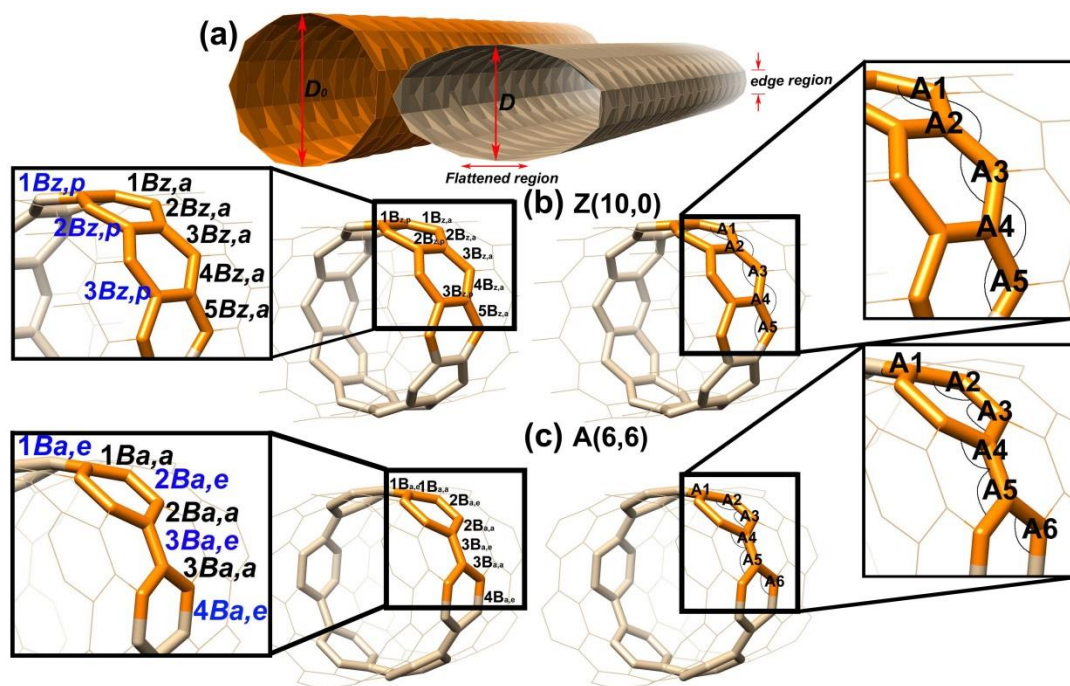


Figure 3. 1: (a) The degree of flatness is calculated as $\eta = (D_0 - D)/D_0$. D and D_0 are the diameters shown in the figure (b, c) Representative SWCNTs, Z(10,0) and A(6,6), with two different bond lengths ($B_{z,a}$, $B_{z,p}$ and $B_{a,a}$, $B_{a,e}$) and a bond angle (A) in a quadrant of the tube colored in orange. 1-5 $B_{z,a}$, 1-3 $B_{z,p}$ and A1-A5 were determined for Z(10,0) and 1-4 $B_{a,e}$, 1-3 $B_{a,a}$ and A1-A6 for A(6,6).

All the calculations were considered converged when the maximum force on the atom was below 0.01 eV \AA^{-1} , maximum stress was below 0.01 GPa , and the maximum displacement between cycles was below 0.001 \AA . The current investigation involved two types of SWCNTs. The zigzag (Z) and the armchair (A) tubes were selected for five different sizes of the diameter. These are Z(10,0), Z(15,0), Z(20,0), Z(25,0) and Z(30,0) for the zigzag tubes and A(6,6), A(8,8), A(10,10), A(14,14) and A(17,17) for the armchair tubes. The tube diameters of both chiral SWCNTs were shown in Table 3.1.

Table 3. 1: The tube diameters of native and deformed SWCNTs and box parameter (γ)

SWCNT	Diameter $r(D_0)/\text{Å}$	γ/degree				
		$\eta = 0.0$	$\eta = 0.1$	$\eta = 0.2$	$\eta = 0.3$	$\eta = 0.4$
Z(10,0)	7.83	120.00	102.30	87.49	74.50	62.50
Z(15,0)	11.74	120.00	103.16	88.28	86.24	62.98
Z(20,0)	15.66	120.00	102.38	87.68	74.61	62.59
Z(25,0)	19.57	120.00	102.25	87.53	74.42	62.37
Z(30,0)	23.49	120.00	102.55	87.79	74.68	62.63
A(6,6)	8.14	120.00	104.68	89.45	75.91	63.67
A(8,8)	10.85	120.00	103.20	87.76	74.03	61.33
A(10,10)	13.56	120.00	101.82	87.02	73.83	61.65
A(14,14)	18.98	120.00	102.36	87.63	74.54	62.49
A(17,17)	23.05	120.00	102.42	87.66	74.53	62.46

3.2 Geometrical structures of the zigzag and the armchair SWCNTs

With respect to the tube axis, bond lengths can be divided into the angular ($B_{z,a}$) and the parallel ($B_{z,p}$) groups for the zigzag SWCNTs (see Figure 3.1b) and the angular ($B_{a,a}$) and equatorial ($B_{a,e}$) groups for the armchair SWCNTs (see Figure 3.1c) based on their topologies and geometries relative to the direction of the circumference. Due to symmetry, some bond lengths and bond angles do not have to be defined or measured. Furthermore, there is no need to define some angles because such an angle and its adjacent ones make up a full angle (360°) and can be easily computed.

3.3 Deformed structures of the SWCNTs

In order to characterize the tube flatness, a dimensionless quantity as, the degree of flatness (η), is defined by $(D_0 - D)/D_0$ as shown in Figure 3.1, where D_0 is the original diameter of an undeformed tube (before applying the force) and D is the minor diameter of the deformed tube (after applying the force). The geometries of the deformed tubes were relaxed in the periodic box by constraining the γ parameter as shown in Table 3.1. For all deformed structures, the degree of flatness (η) was increased from 0.0 to 0.4 with the interval value of 0.1. At a fixed η , other parameters representing the molecular geometry of SWCNTs were fully optimized. The bond length and angle were measured for all deformed structures of both SWCNTs.

3.4 Ab initio pseudopotentials method

All system preparations and calculations of SWCNTs under periodic boundary conditions were initially generated and optimized using the CASTEP module implemented in Material Studio 5.5 program [60]. Density functional calculations were performed on each structure using the plane-wave pseudopotential method within the generalized gradient approximation (GGA) with Perdew, Burke and Ernzerhof (PBE) correlation. Ultrasoft pseudopotential is used to model the ion-electron interaction. The cutoff energy for the plane-wave basis is chosen to be 300 eV. Consequently, the structure in the periodically repeating tetragonal cell, $\alpha = \beta = 90^\circ$ and $\gamma = 120^\circ$, was used in the optimization of the structures for all systems. Finally, the energy band gaps were recorded.

3.5 Model of the graphene oxide and optimization

The graphene oxide structure based on the Lerf-Klinowski model [63] contains oxygen atoms on the graphene surface (54 carbon atoms) in the forms of epoxy,

hydroxyl and carboxyl groups. This model consists of epoxy (C-O-C), hydroxyl (-OH), double bond (C=C) and carbonyl (-C=O) groups integrated on the graphene sheet. The C/O ratio can be approximately 4:1-2:1 in most cases [64]. The number of functional groups on the graphene sheet is consistent with the C/O ratio from the previous works [43, 65]. The Lerf-Klinowski model is the most reasonable structural model for the GO system in the present study the C/O ratio is 3.0:1 as shown in Figure 3.2. Experimentally, Casabianca *et al.* [65] showed a comparison of the experimental spectrum with the simulated spectra that the model based on the Lerf-Klinowski model best matched the experimental spectrum with compared to other suggested models.

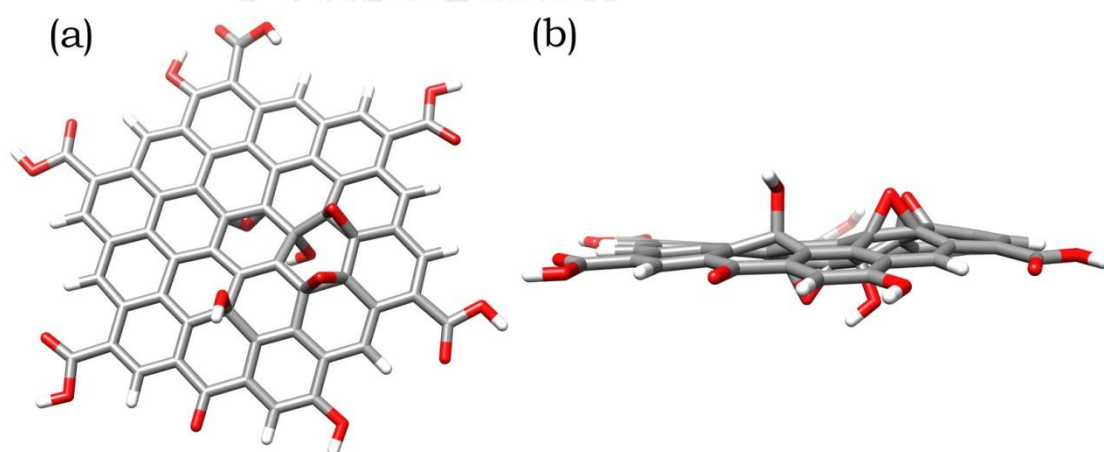


Figure 3. 2: (a) Top and (b) side views of schematic representation of graphene oxide model

Structure of $M^{2+} \dots GO$ complexes was generated by including all possible types of adsorption position (Figure 3.3).

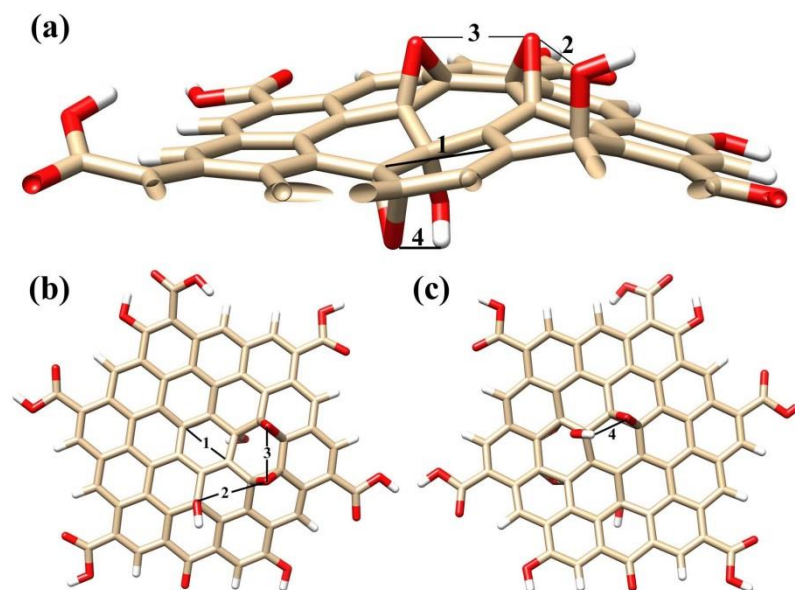


Figure 3.3: (a) The four adsorption sites, 1-4, of GO surface for each ion (b) Top view of GO surface where 1 is the ion position at the center of GO, 2 is the position between the epoxide and hydroxyl group and 3 is the position at the center of two epoxide groups. (c) Bottom-up view of GO surface where 4 is the ion position between the epoxide and hydroxyl group. Note that the metal ion is placed above the surface by 5 \AA on each side.

In this GO system, the positions of the functional groups were three points at top of surface and one point at bottom of surface (Figure 3.3). To study cation adsorption on GO surface, binding energy of metal cation on the GO was determined at the 4 different positions. The positions 1-3 were at the top of GO sheet, while the position 4 was at the bottom of GO sheet. Position 1 was placed at the GO center without any functional group. Position 2 was at between the epoxide and hydroxyl groups. The position 3 was located between the two epoxide groups. Lastly, the position 4 was opposite to position 1 at the bottom of GO sheet with nearby the epoxide and hydroxyl groups.

All geometry optimizations were performed with density-functional-theory (DFT) B3LYP, and meta-hybrid DFT M06 with the 6-31g(d) basis set. In addition, the counterpoise corrections were applied to eliminate basis set superposition error (BSSE). The obtained interaction energies of each metal cation at the 4 different positions on GO surface. Rungrim *et al.* [66] investigated the size effect of graphene sheet on the nucleobase binding. They found that the coronene (C24) was too small and the edge effect may perturb the binding of nucleobases. Therefore, the size of graphene sheet suitable for the adsorption of nucleobases should be larger than C24 or at least around 54 carbon atoms [67]. This is therefore in this work, the C54 sheet was selected to model the GO sheet for the study of the cation adsorption. The optimized structures by present basis sets such as 6-31g(d), cc-pVDZ and cc-pVTZ, the distances between heavy atoms of drugs and carbon atoms of graphene are quite similar [66]. Therefore, we adopted the 6-31g(d) basis set to calculate the binding energies of metal cations on GO surface. In this work we performed the CP BSSE calculations with the standard LANL2DZ (Los Alamos National Laboratory 2 Double-Zeta) pseudopotential and also a modified ECP aiming to improve the divalent metal atom basis set [68]. More sophisticated basis sets have been developed for use in highly accurate calculations with correlated methods [69].

3.6 Binding energy calculations of GO complexes

The graphene oxide structure contains the epoxy, hydroxyl and carboxyl groups on the graphene surface (C54). These functional groups located of graphene oxide at center. The GO model in this work has 2 epoxy and 1 hydroxyl groups on one side, 1 epoxy and 1 hydroxyl groups on another side, and 5 carboxylic acid, 2 hydroxyl and 1 carbonyl groups at the edge of GO. The graphene oxide was fully optimized by B3LYP

and M06 with 6-31g(d) level of theory. The adsorption energies of the divalent metal ions-GO systems were calculated by using B3LYP and M06 methods with 6-31g(d) level of theory for oxygen, carbon, and hydrogen atoms and effective core potential (ECP) basis set, LANL2DZ was used for M^{2+} . The interaction energy was then corrected by basis set superposition error (BSSE) using the counterpoise correction (CP) [70]. In this study, the focused M^{2+} ions were Cd^{2+} , Cu^{2+} , Hg^{2+} and Zn^{2+} . Each ion was located above the center and perpendicular to functional groups on the graphene oxide sheet (Figure. 3.3) and then the complex geometries were fully optimized using the B3LYP and M06 with 6-31g(d) level of theory. All calculations were performed with the GAUSSIAN 09 quantum chemistry software package [71], which has been expanded to include a number of DFT methods. The binding energy of complexes is defined by

$$\Delta E_{bind} = E_{cpx} - E_{GO} - E_{M^{2+}} \quad (3.1)$$

Where E_{cpx} , E_{GO} and $E_{M^{2+}}$ the energies of the optimized complex, GO and M^{2+} , respectively.

CHAPTER IV

RESULTS AND DISCUSSION

4.1 Single-walled carbon nanotubes (SWCNTs)

4.1.1 Validation of density functional theory (DFT) methods for SWCNTs

To validate the DFT methods for the calculation of the energy band gaps in the normal and deformed of SWCNTs, we first applied the different methods, LDA, GGA, HF, PW91, PBE0 and B3LYP in comparison with the experimental results in Table 4.1. It can be seen that the PBE0 well predicted energy band gaps of the zigzag and armchair SWCNTs relatively in correspondence to the experiment data [3, 72-74]. Therefore, the PBE0 method was chosen for study on the energy band gap of normal and deformed SWCNTs.

Table 4. 1: Method validation compared between calculated and experimental values for zigzag and armchair of normal SWCNTs in terms of band gap (eV)

Type	LDA	GGA	HF	PW91	PBE0	B3LYP	Exp.
Z(9,0)	0.024	0.5 ^[75]	0.818	0.249	0.017	0.079 ^[76]	0.080±0.005 ^[72]
Z(10,0)	0.9 ^[38]	0.92 ^[37]	3.612	0.8 ^[3]	1.253	1.251	1.1 ^[3]
Z(15,0)	0.0 ^[75]	0.0 ^[75]	0.520	0.00	0.014	0.036	0.029±0.0054 ^[72]
A(6,6)	0.0 ^[77]	2.0 ^[78]	0.940	0.369	0.000	0.000	0.0 ^[74]
A(8,8)	0.0 ^[79]	1.55 ^[78]	1.405	0.249	0.224	0.994	0.1 ^[72]
A(10,10)	0.0 ^[79]	0.25 ^[80]	1.465	0.219	0.152	0.00 ^[76]	0.08-0.1 ^[72]

4.1.2 Effect of applied force on bond lengths of SWCNTs

Based on the optimized structures of normal and deformed SWCNTs with plane-wave pseudopotential calculations using the PBE method, due to the tube symmetry, the C-C bond lengths and C-C-C bond angles of zigzag and armchair tubes in a quadrant region (Figure. 3.1b and 3.1c) were measured. By considering the structure in accordance with tube axis, the bond lengths can be divided into angular ($B_{a,p}$) and parallel ($B_{z,p}$) groups based on their topologies and geometries relative to the direction of the circumference. The C-C bond lengths were monitored from the optimized structures of the SWCNTs under normal conditions and applied forces as shown in Figure. 4.1.

It can be seen that under applied force each chiral tube has its own unique characteristic of structural change. In zigzag SWCNTs (Figure. 4.1, left), the bond lengths in $B_{z,p}$ type, which are in direction parallel to the tube axis, were kept constant at 1.42 Å in correspondence to the elliptical zigzag SWCNTs under hydrostatic pressure [21]. In contrast, the applied forces had affected almost all B bond lengths with the same pattern in the five different sizes of zigzag tubes. For all zigzag tubes, increased η from 0.1 to 0.4 has dramatically enhanced the bond length at the highest point of flattened region (1.68 Å, 1.88 Å, 2.04 Å and 2.17 Å) but decreased the bond length at edge region on x axis (1.32 Å, 1.22 Å, 1.13 Å and 1.04 Å). The bond length at the middle of the tube was continually decreases in correspondence to the circumference.

Most notably, this is the first study on investigation of the effectiveness of applied force to SWCNTs. For example, at high pressure ($\eta = 0.4$) the slope was a rapidly negative decrease, while, at low pressure ($\eta = 0.1$) the slope was a slowly negative decrease. The critical point of bond length change was found at

approximately at the middle of the tube. It is the bond length of zigzag SWCNTs all conformation have been a same C-C bond length are in 1.42 Å. That mean, even though forces to the zigzag SWCNTs have been applied the bond length was kept constant. This might involve that a part of the tube was not influenced by the applied force.

For metallic armchair tubes (Figure. 4.1, right), both $B_{a,e}$ and $B_{a,o}$ bond lengths were influenced by force applied. Referred to the axial and the equatorial bonds strongly effects the tube flattening regions these two types of bonds were observed (Figure. 4.1). For the bond length perpendicular to the tube axis, $1B_{a,e}$ - $3B_{a,e}$ at the edge region (see Figure. 3.1a for the definition) were dramatically changed as a function of tube flattening. At the highest flattened region, as a function of the flatness η , the $1B_{a,o}$ (1.82, 2.01, 2.23 and 2.40 Å) was more significantly lengthened than the $B_{a,e}$ (1.51, 1.57, 1.64 and 1.69 Å). Similarly at the edge region, the $B_{a,o}$ bond lengths were also affected rather than the $B_{a,e}$ bond lengths. For example at $\eta = 0.4$ in A(6,6), $3B_{a,o}$ is equal to 1.33 Å while $4B_{a,o}$ is of 0.86 Å. From these results, the force has larger influence on $B_{a,e}$ than on $B_{a,o}$. Therefore, the geometry at edge parts is influenced more than the geometry at the flattened parts. The C-C bond lengths at the edge part are shorter than that in graphite. It has been concluded that the local sp^2 hybridization was partially destroyed due to the deformation of SWCNTs.

By taking into account the effect of flattening shown in Figure. 4.1, the data suggested us to conclude, interestingly, that flattening of the tube cross-section leads to dramatic changes of the C-C bond length at the edge region, elongation of the C-C bonds that lie parallel, and vice versa for those perpendiculars, to the tube axis. In

addition, this also affects a significant increase of the C-C bond lying parallel to the tube axis in the flattened region.

The previous work has shown the effect of uniaxial strain on the structures of SWCNTs, with the finding that bond lengths along the axis were increased [81]. However, the results were different from those for zigzag SWCNTs obtained by Pullen *et al* [81]. For zigzag SWCNTs, two types of bond lengths (defined as angular and parallel bonds in Figure 3.1b) were found to change significantly. Moreover, for a given size of the nanotube, there was always a critical bond length that remained constant despite the change in pressure. This implies that parts of the tube may not be influenced by the applied forces. Similarly, for armchair SWCNTs, two types of bond lengths (defined as angular and equatorial bonds in Figure 3.1c) changed significantly, with dramatic increases and decreases of the equatorial and angular bonds, respectively, with a very weak external force.

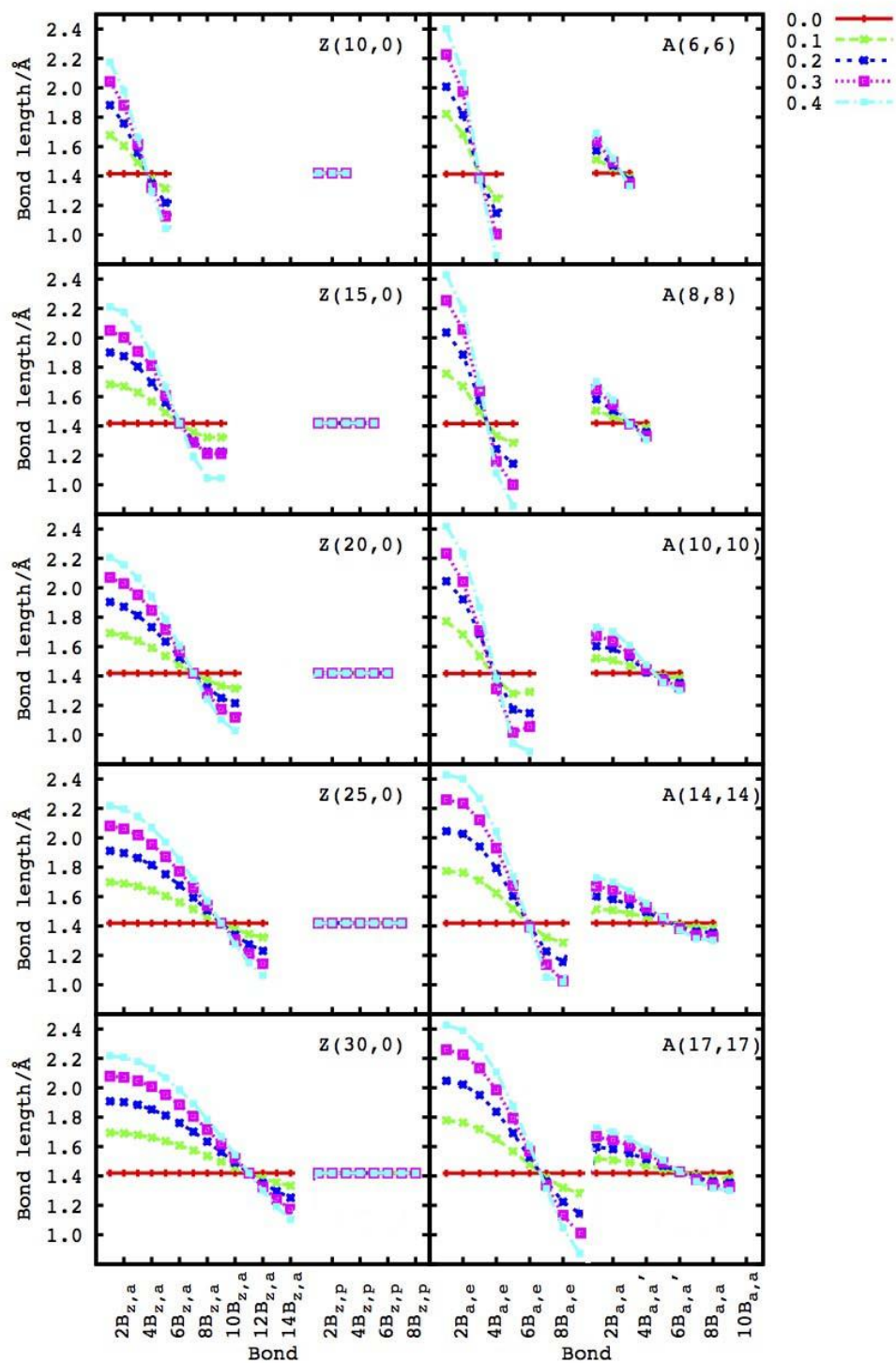


Figure 4. 1: Variation of C-C bond lengths, $B_{z,a}$ and $B_{z,p}$ (defined in Figure 3.1b) for zigzag (10,0), (15,0), (20,0), (25,0) and (30,0) SWCNTs, and $B_{a,a}$ and $B_{a,e}$ (defined in Figure 3.1c) for armchair (6,6), (8,8), (10,10), (14,14) and (17,17)SWCNTs as a function of flatness (η)

4.1.3 Effect of applied force on bond angle of SWCNTs

The C-C-C bond angles ($A1, A2, A3, A4, \dots$) were defined in Figure. 3.1b and 3.1c. For example, there are five and six bond angles in the structure of the zigzag Z(10,0) and the armchair A(6,6) tube, respectively. The angle numbers depend on the size of the tube. For the zigzag SWCNTs, the $A1$ angles at the flattened region were increased from 120° ($\eta=0.0$) to $128^\circ, 134^\circ, 138^\circ$ and 140° for η equal to 0.1, 0.2, 0.3 and 0.4, respectively. Although the angle changes in all zigzag tubes were in the same trend, the angles at the edge region were less affected when the size of the tube increased. The bond angle at the flattened region of the zigzag tube was higher than that of the armchair tube. The bond angles at the flattened and edge regions of the armchair tube are influenced by pressure and follow the same trend. The applied forces affected the bond angles at the flattened and edge regions with the same pattern in the armchair tube. C-C-C bond angles at the edge gradually decreased as a function of tube flattening, *i.e.*, from 117° to 108° when the degree of flattening (η) changed from 0.0 to 0.4. In contrast, the edge region angles $A4$ and $A5$ significantly decreased when flatness increased ($\eta = 0.4$). This is in contrast to the observations in the flattened region in which $A4$ and $A5$ were significantly decreased when the flattening increased ($\eta = 0.4$). The higher slope in Figure. 4.2 (left) demonstrate that the angle of zigzag tubes was affected by increased η more than the armchair tube. For example, the Z(10,0) for the angle gap is 40° but the A(6,6) for the angle gap is 10° . The bond angle of Z(10,0) at the flattened region ($A1$) is 140° but for A(6,6) it is 130° for $\eta = 0.4$. The bond angles along axial edge parts A ($A1-A3$) of zigzag tube increases, while those of the equatorial flattened parts ($A4-A5$) decreased when the degree of flattened (η) increases. Therefore, the angles at flattened and edge regions were larger and smaller

than those of graphite. At this point, the bond angle is constant at about 120° for all η flatness values. Overall, we conclude that local sp^2 hybridization was partially destroyed due to deformation of SWCNTs.

4.1.4 Effect of applied force on electronic properties of SWCNTs

As mentioned previously, the aim of this work was to investigate the effect of pressure on the electronic structure of the SWCNTs in term of the energy band gap. The energy band gaps of zigzag and armchair tubes as a function of flatness (η) were displayed in Figures 4.3 and 4.4. The energy values obtained from plane-wave methods were compared with the experimental data. Again, the energy band gap for the zigzag and armchair SWCNTs are summarized in Table 4.2 for clarification. The energy band gaps of the normal ($\eta=0.0$) were 1.251 and 0.014 eV of Z(10,0) and Z(15,0) SWCNTs, respectively, in relatively closed to the experimental values (1.1 eV [3] and 0.036 eV [72]). As a function of flatness (η), the energy band gap of Z(10,0) was quickly decreased when the flatness increased from 1.251 eV to 0.296 eV at $\eta = 0.1$ and to 0.106 eV at $\eta = 0.4$. This behavior showed that the electronic property of metallic tube has been changed to semiconductor. While the energy band gap of Z(15,0) was increased from 0.014 eV to 0.650 eV at $\eta = 0.1$ and to 0.668 eV at $\eta = 0.4$. It is evident that the electronic property of semiconductor has been changed to be metallic instead. The curvature effect, as one result of the geometry properties, can significantly affect the electronic structure of SWCNTs [82]. The difference between the two π bond of the nanotube diameter decreases. This π bond is shifted down even further to closely each other, leading to metallic properties for this nanotube.

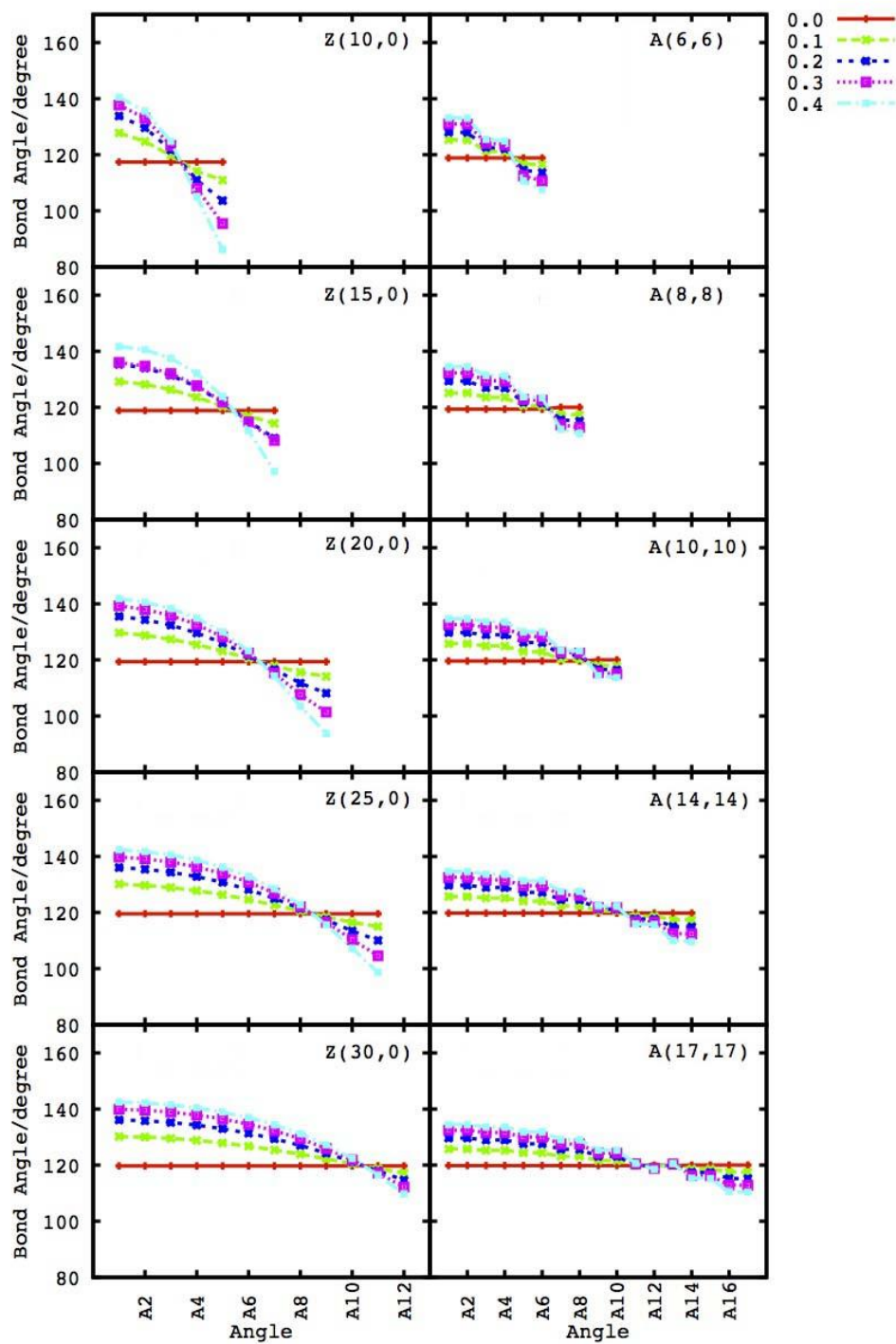


Figure 4. 2: Variation of C-C-C bond angles, A (defined in Figure 3.1b) for zigzag (10,0), (15,0), (20,0), (25,0) and (30,0) SWCNTs, and for armchair (6,6), (8,8), (10,10), (14,14) and (17,17) SWCNTs as a function of flatness (η)

Table 4. 2: Energy band gap (eV) for normal and deformed zigzag and armchair SWCNTs with five different η values.

η	Energy band gap/eV									
	zigzag tube					armchair tube				
	(10,0)	(15,0)	(20,0)	(25,0)	(30,0)	(6,6)	(8,8)	(10,10)	(14,14)	(17,17)
0.0	1.251	0.014	0.114	0.170	0.002	0.000	0.224	0.152	0.000	0.000
0.1	0.296	0.650	0.000	0.042	0.071	1.736	1.605	1.388	1.240	1.060
0.2	0.217	0.585	0.194	0.001	0.013	1.111	1.140	0.385	0.225	0.107
0.3	0.267	0.614	0.000	0.000	0.000	0.000	0.000	0.000	0.000	0.000
0.4	0.106	0.668	0.000	0.000	0.000	0.000	0.000	0.000	0.000	0.000
B3LYP/DURAND_21G*	-	0.036 ^[76]	-	-	0.0 ^[76]	-	-	0.0 ^[76]	-	-
($\eta = 0.0$)										
Exp. ($\eta = 0.0$)	1.1 ^[5]	0.029±0.004 ^[72]	-	-	-	-	0.1 ^[83]	0.0 ^[72]	-	-

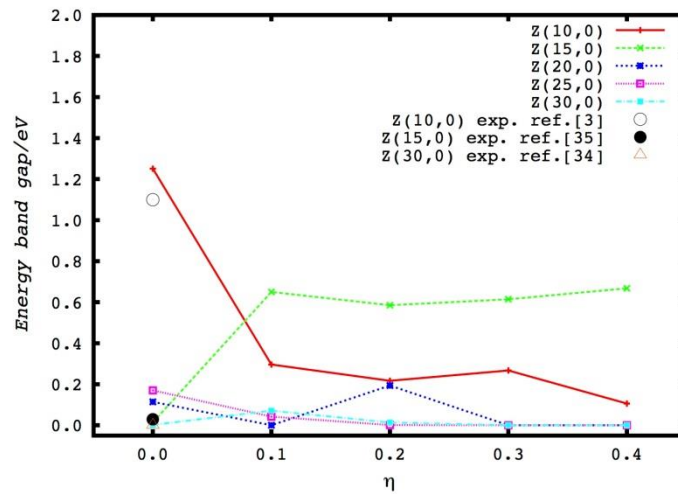


Figure 4. 3: Energy band gap (eV) of the zigzag (10,0), (15,0), (20,0), (25,0) and (30,0) SWCNTs as a function of flatness (η)

On the other hand, the energy band gap rapidly increased with increasing the flatness at $\eta = 0.1$ for all armchair SWCNTs. Afterwards, the energy band gap was decreased immediately and finally reached to 0.0 eV at high η values (0.3 and 0.4). For example, the energy band gap of the normal A(8,8) and Z(10,10) SWCNTs were 0.224 eV and 0.152 eV, respectively, somewhat in a good agreement with experimental data (0.1 eV [83] and 0.0 eV [76]). Therefore, the metallic properties of the armchair SWCNTs can easily become the semiconductor when the flatness (η) increased. A significant decrease of the energy gap as a function of the external force was found.

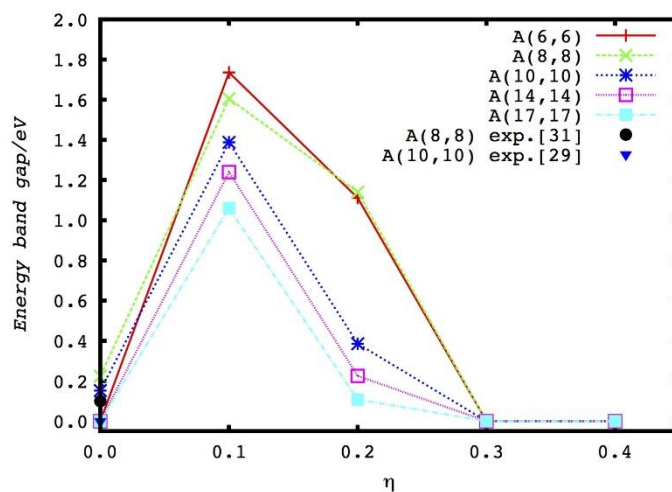


Figure 4. 4: Energy band gaps (eV) of the armchair (6,6), (8,8), (10,10), (14,14) and (17,17) SWCNTs as a function of flatness (η)

These results lead to the clear and interesting conclusion that the effects of external forces are much stronger on the flattened region of the nanotube, with the local bonding change from sp^2 to almost sp^3 [84]. In particular, the σ^* - π^* hybridization effect [85] becomes a key factor in gap closure before layer-layer interactions start to grow. The armchair results are pertinent to those obtained by Mazzoni *et al.* [37].

4.2 The divalent metal cations adsorption on graphene oxide

4.2.1 Validation of calculation method for metal-GO complexes binding energies

To validate the calculated method used in this study, the different method with various basis set were used. The binding energies (ΔE_{bind}), and the corresponding binding distances (R) for the cation-benzene complexes are summarized in Table 4.3. Moreover, the calculated results with the same system [86, 87] were referred and shown as well as the ΔH from experiment were also indicated [86-89]. Note that, in each case, R was measured from the center of mass of the benzene ring to the metal cations.

In Table 4.3, the binding energies and the binding distances obtained from the B3LYP/6-31g(d) with LANL2DZ level of accuracy are in good agreement with the experimental values [86-89]. In the case of geometry, the binding distance was in agreement with the previous study [86, 87]. Therefore, the B3LYP/6-31g(d) with LANL2DZ level was chosen for this study.

4.2.2 Binding energies of the divalent metal cations on GO sheet

The x and y axis pass through the center of GO sheet and x axis passes to the oxygen atom of the carboxylic functional group (blue atom). The coordinate plane passes the four reference points linked to carboxylic acids on the GO sheet (as seen a green plane in Figure 4.5). The configurations of the complexes were modeled by placing the M^{2+} at above the center and perpendicular to the functional groups as illustrated in Figure 4.5. The complex geometries were fully optimized using the B3LYP/6-31g(d)/LANL2DZ basis set.

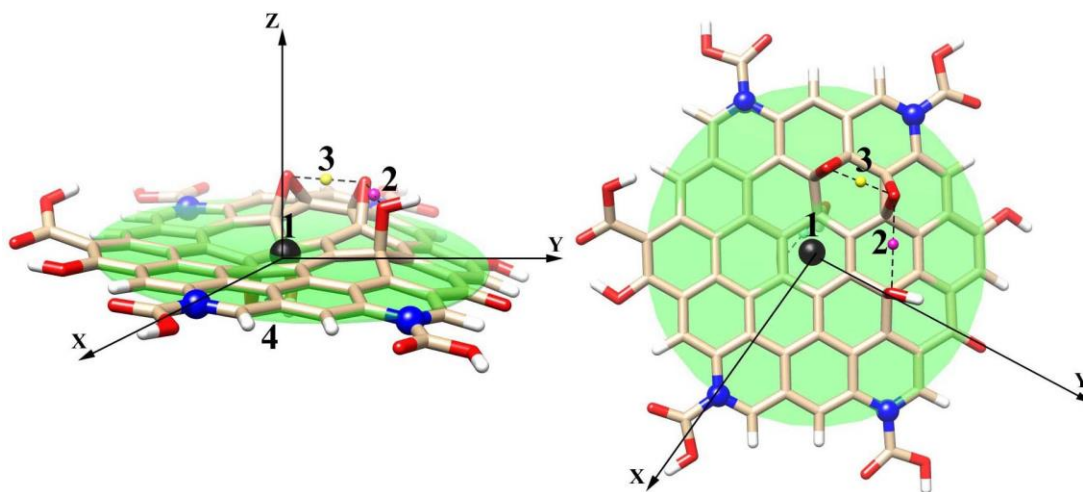


Figure 4. 5: Model of grapheme oxide (GO) sheet used in this study. Plane of the GO sheet (green) and the four positions (1-4) for metal cation adsorption

The structures of metal cations and GO, were performed by the B3LYP method with 6-31g(d)/LANL2DZ basis set. An improved effective core potential for the metal atom (ECP) [90] was combined with the 6-31g(d) basis set. The binding energies with BSSE corrections in parenthesis of the divalent metal cations with graphene oxides (GO) using the four initial ion positions are presented in Table 4.4.

The ΔE_{bind} values of all studied complexes were decreased by $\sim 3-7$ kcal/mol after the BSSE corrections in which similar to what found in many systems [91]. In this study, the GO model contained the epoxy and hydroxyl groups on the graphene sheet where each divalent cation was initially placed at the positions 1-4. Note that, the interaction of the divalent metal ion with GO with various functional groups favorably found at the binding sites of C-O-C and OH groups [92]. From Table 4.4, the order of binding strength of cation-GO systems on the top of GO sheet were chosen from the lowest energies of each metal cations (among the initial positions 1-4) was Cu^{2+} (-361.91) > Zn^{2+} (-281.06) > Hg^{2+} (-277.52) > Cd^{2+} (-241.24), with BSSE correction.

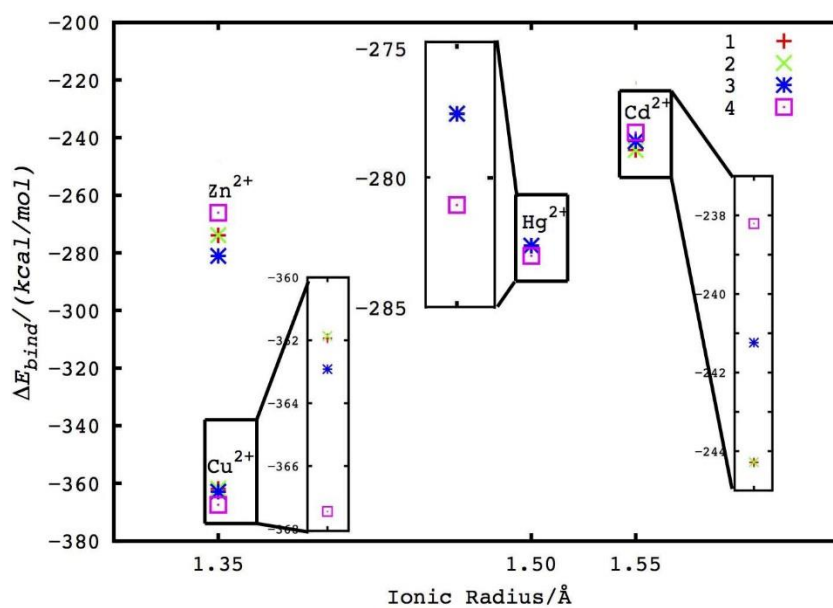


Figure 4. 6: The binding energy (ΔE_{bind}) of four divalent metals with 4 positions at B3LYP/6-31g(d)/LANL2DZ basis set.

In addition, the binding energy of Cu²⁺ on the GO sheet was much lower than those of Hg²⁺, Cd²⁺ and Zn²⁺, in correspondence with the shorter binding distance (d of 0.62 Å).

Table 4. 3: Binding energies (ΔE_{bind}), derived according to Eq.3.1, for the benzene-cation (Cd^+ , Cu^+ , Hg^+ , Zn^+ and Ag^+) obtained from this work and the previous studies. The distance (R) was measured from the center of mass or the nearest atom of the benzene ring to the metal cation.

Methods	Basis set	ΔE_{bind} (kcal·mol ⁻¹)					R(Å)				
		Cd^+	Cu^+	Hg^+	Zn^+	Ag^+	Cd^+	Cu^+	Hg^+	Zn^+	Ag^+
B3LYP	LANL2DZ	-34.94	-51.41	-38.45	-30.48	-41.96	2.44	1.93	2.77	2.29	2.30
	au ζ -cc-pVQZ-PP	-36.90	-61.83	-55.95	-41.31	-41.31	2.56	1.79	2.78	2.34	2.39
	au ζ -cc-pVTZ-PP	-40.16	-57.97	-55.62	-35.65	-47.26	2.54	1.80	2.79	2.34	2.34
M06	LANL2DZ	-40.13	-58.28	-40.61	-39.36	-43.30	2.54	1.88	2.76	2.24	2.32
	au ζ -cc-pVQZ-PP	-40.57	-64.15	-56.99	-48.10	-48.10	2.51	1.70	2.79	2.33	2.57
	au ζ -cc-pVTZ-PP	-36.36	-62.71	-56.36	-47.25	-47.47	2.50	1.72	2.79	2.34	2.36
MP2	LANL2DZ	-31.49	-34.59	-36.85	-39.36	-26.85	2.44	1.96	2.75	2.19	2.35
CCSD(T)	LANL2DZ	-31.50	-37.35	-36.80	-36.81	-26.70	2.44	1.96	2.50 ^[86]	2.19	2.35
MP2	LANL2DZ	-32.51 ^[87]	-	-	-	-38.74 ^[87]	2.44 ^[87]	-	-	-	2.27 ^[87]
ΔH (Experiment)		-32.51 ^[87]	-52.10 ^[88]	-38.18 ^[86]	-	-37.28 ^[89]	-	-	-	-	-

Table 4. 4: Summary of calculated results for divalent metal adsorption on graphene oxide: the distance (d), the curvature distances (h) (in terms of the shortest distance between the metal atom and the GO plane) [\AA] and binding energy; ΔE_{bind} ($\text{kcal}\cdot\text{mol}^{-1}$) of the divalent metal adsorption on GO surface with and without BSSE corrections by using 6-31g(d) basis set. The values in parentheses are the binding energies with BSSE correction. The value in blanket under metal ion is an ionic radius (\AA). The bond distances ($r_{\text{O1-O3}}$) were measured from projection point to the oxygen atom of functional groups [\AA]. The bond distance ($l_{\text{O1-O3}}$, $l_{\text{O1-O2}}$ and $l_{\text{O2-O3}}$) was measured from an oxygen atom to another oxygen atom of functional groups [\AA], and the angle (θ) in term of the angle between the O1-O2-O3 plane and the GO plane [degree]

Metal	positions	r_{O1}	r_{O2}	r_{O3}	$l_{\text{O1-O3}}$	$l_{\text{O1-O2}}$	$l_{\text{O2-O3}}$	θ	d	h_1	h_2	ΔE_{bind}
Cd^{2+} <1.55>	1	0.544	2.476	2.918	3.227	2.584	4.675	6.440	1.439	0.559	0.605	-248.86(-244.29)
	2	1.094	2.638	2.688	3.358	2.609	4.817	5.272	1.066	0.634	0.490	-246.08(-241.24)
	3	0.546	2.476	2.917	3.226	2.585	4.674	6.436	1.437	0.559	0.605	-248.85(-244.28)
	4	8.062	6.808	7.806	3.451	2.568	4.962	5.180	-6.635	0.850	0.382	-239.69(-238.21)
Cu^{2+} <1.35>	1	1.273	2.740	2.391	3.240	2.596	4.571	5.865	0.618	0.418	0.693	-369.74(-361.94)
	2	1.274	2.735	2.393	3.238	2.595	4.568	5.867	0.617	0.416	0.695	-370.24(-362.92)
	3	1.273	2.740	2.393	3.241	2.595	4.572	5.864	0.619	0.419	0.692	-369.69(-361.86)
	4	7.297	5.793	7.513	3.456	2.581	4.977	5.325	-4.862	0.899	0.563	-371.73(-367.44)
Hg^{2+} <1.50>	1	0.459	2.997	3.234	3.470	2.571	4.983	5.342	2.710	0.847	0.354	-280.31(-277.53)
	2	0.461	3.000	3.232	3.470	2.572	4.983	5.323	2.707	0.846	0.355	-280.31(-277.52)
	3	0.455	2.993	3.225	3.470	2.571	4.983	5.312	2.700	0.847	0.355	-280.30(-277.50)
	4	6.594	5.705	6.116	3.443	2.568	4.959	5.286	-7.041	0.856	0.377	-282.13(-281.04)
Zn^{2+} <1.35>	1	0.684	2.269	3.062	3.239	2.586	4.700	6.036	1.138	0.576	0.573	-280.36(-273.89)
	2	1.240	2.517	2.776	3.354	2.634	4.792	4.884	0.653	0.572	0.487	-288.43(-281.06)
	3	0.692	2.271	3.055	3.239	2.587	4.698	6.018	1.132	0.576	0.574	-280.36(-273.88)
	4	7.709	6.568	7.343	3.448	2.568	4.959	5.230	-6.535	0.852	0.383	-267.78(-266.10)

4.2.3 Structural properties of divalent metal cations on GO sheet

The rational goal of this study is focused on the behavior of divalent metal cations on GO sheet, therefore, we evaluated the optimized parameter of GO complexes as the binding distance (R) and an angle β in which defined as the angle of $O-M^{2+}-O$ (Figure 4.7), after the full optimization was performed. The binding distance ($R_{1,2,3}$) is the distance between metal cation and the functional groups including two epoxy and one hydroxyl groups on the surface of GO sheet as illustrated in Figure 4.7. The corresponding binding distance ($R_{1,2,3}$) as well as angle β were reported in Table 4.5. The obtained binding distance, R , of Cd^{2+} , Cu^{2+} , Hg^{2+} and Zn^{2+} are 2.323, 2.124, 3.240 and 2.093 Å, respectively.

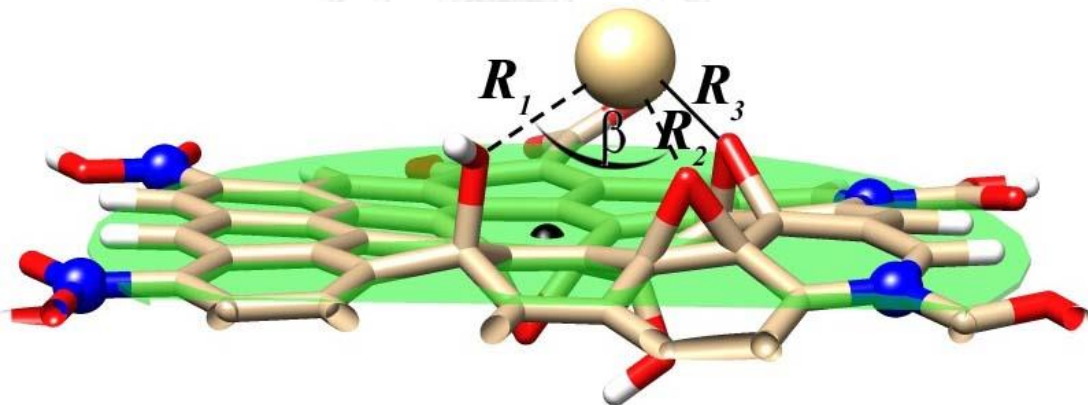


Figure 4. 7: The angle (β) and distances (R_1-R_3) of divalent metal cation adsorption on functional groups of GO sheet

Table 4. 5: Binding distance, R (Å) and angles (β) and (φ) between the divalent metal cation and GO surface

Metal	positions	R_1	R_2	R_3	β	φ
Cd ²⁺	1	2.323	2.533	2.967	59.98	45.75
	2	2.411	2.636	2.686	58.91	57.80
	3	2.323	2.533	2.965	60.00	45.78
Cu ²⁺	1	2.124	2.561	2.184	58.15	64.33
	2	2.125	2.556	2.186	58.11	64.43
	3	2.124	2.561	2.186	58.10	64.28
Hg ²⁺	1	3.242	3.583	3.783	58.59	28.52
	2	3.240	3.583	3.779	58.57	28.53
	3	3.240	3.578	3.774	58.59	28.74
Zn ²⁺	1	2.093	2.215	3.023	60.41	53.38
	2	2.180	2.363	2.637	59.06	68.51
	3	2.094	2.217	3.015	60.40	53.53

From Table 4. 5, we found evidence to suggest that the Cu²⁺ cation has most strongest interact with oxygen atom of functional groups. The distance, (R_2) of the Cu²⁺ cation is 2.124 Å as agreement with the previous study in term of transition metal bound to benzene [93] and from x-ray experiment [94] is 1.97 Å. It is evident that the smaller cation can approach closer to the GO sheet than larger ones and so the order of these distances is consistent with that of the ΔE_{bind} values, namely Cu²⁺ > Zn²⁺ > Hg²⁺ > Cd²⁺. In the majority of cases, for Cu²⁺ and Hg²⁺ have only one point on xy-plane of the GO sheet after optimization. Therefore, these have the binding energies only one value. For Zn²⁺ and Cd²⁺ have two points on xy-plane of the GO sheet after optimization. As can be seen, these have the binding energies more than one value.

For more understanding insight into the structural properties of complexes, three additional parameters, namely, distance (d), angle (θ) and angle (φ) are defined as in Figure 4.8-4.10, respectively and examined. The projection distance (d) represents the shortest distance measured from the metal cation located perpendicular to the O_1 - O_2 - O_3 plane (Figure 4.8). The plane angle (θ) is defined by the angle between the plane of oxygen functional groups and reference plane of a GO surface (Figure 4.9). The angle (φ) is defined as the angle between two planes, one is O_3 -com- O_1 (com: center of mass between O_3 and O_1) plane as perpendicular to the GO plane (green plane) and another one is O_3 - M^{2+} - O_1 plane (red plane) (see Figure 4.10).

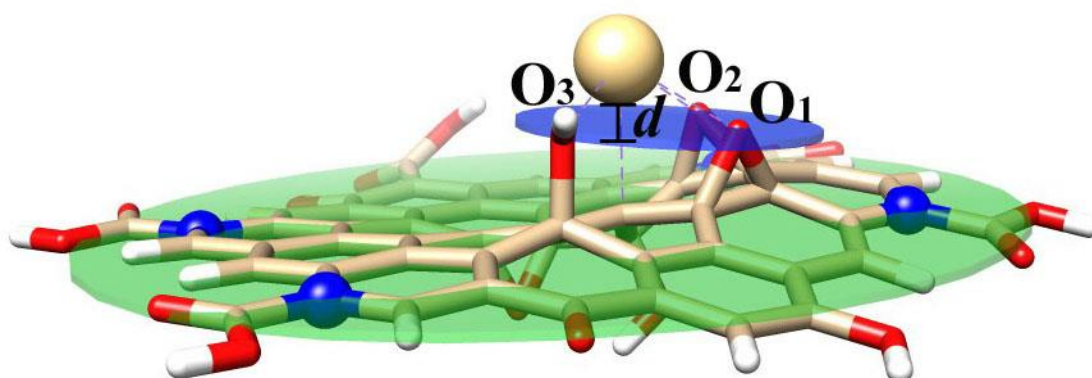


Figure 4. 8: Definition of the distance (d) measured from the divalent cation to the O_1 - O_2 - O_3 plane

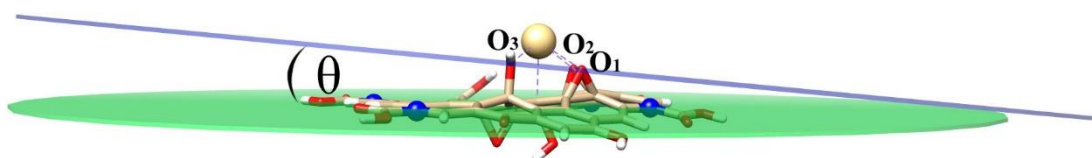


Figure 4. 9: Definition of the angle (θ) between the O_1 - O_2 - O_3 plane and the GO plane

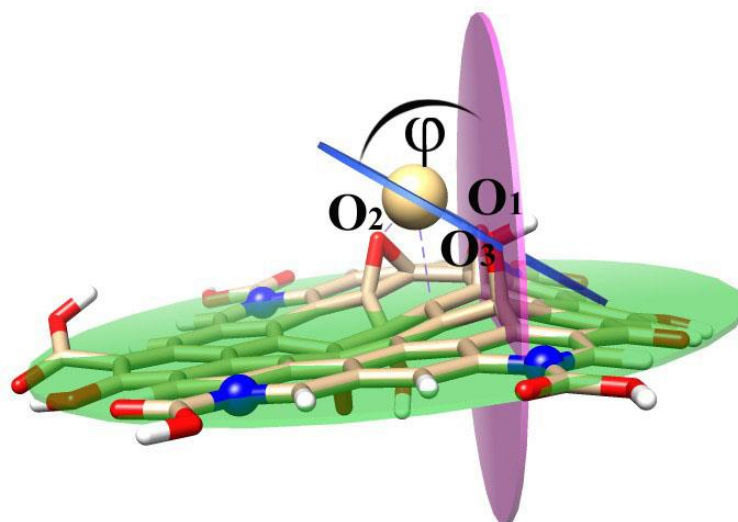


Figure 4. 10: Angle (ϕ) measured between two planes.

To study the angle of the complex geometry on the cation interaction, the angle (θ) for the Cd^{2+} , Cu^{2+} , Hg^{2+} and Zn^{2+} cation complexes were summarized in Figures 4.11 and Table 4.4.

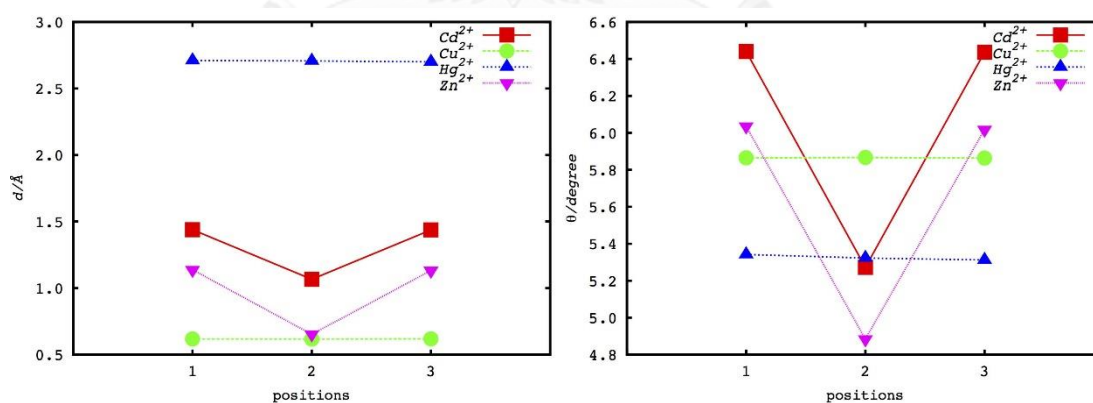


Figure 4. 11: The projection distance (d) and angle (θ) of M^{2+} -GO complexes with 3 positions at B3LYP/6-31g(d).

Comparing Figure 4.12 and Table 4.4 shows that the angle (φ) can confirm the location of the metal cations on the GO surface. In term of the angle (φ), there is only Cu^{2+} and Hg^{2+} cations have a constant angle value.

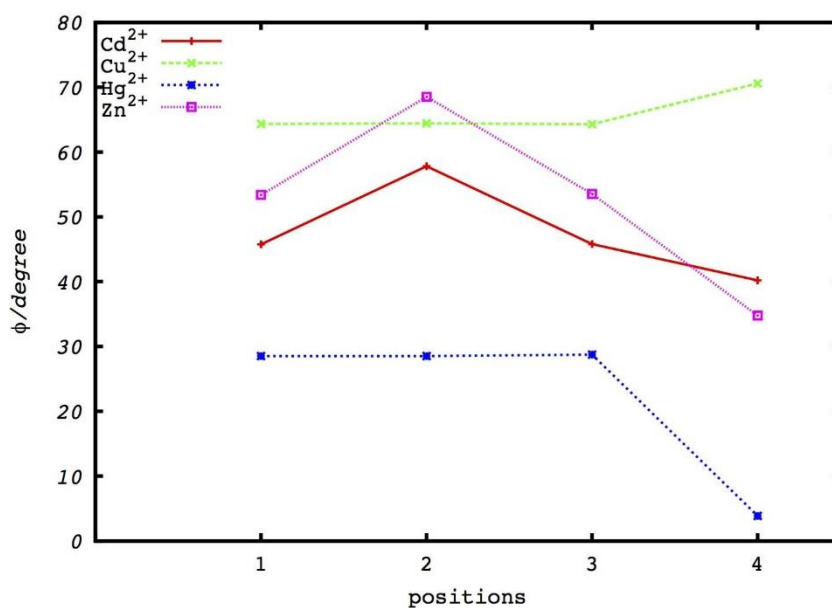


Figure 4. 12: The angle (φ) of divalent metal cations adsorption on plane reference of functional groups.

4.2.4 Investigation the behavior of the divalent metal cations on the graphene oxide

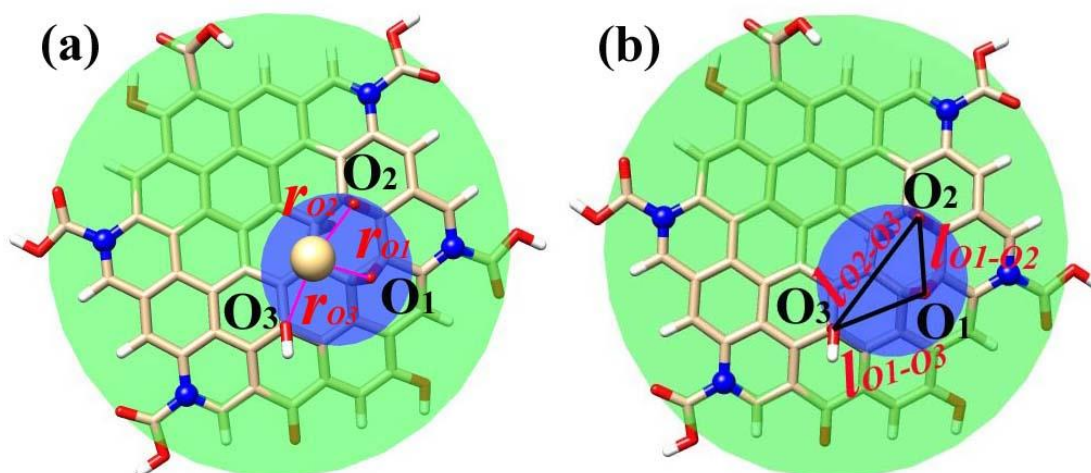


Figure 4. 13: (a) The distance (r_o), and (b) O-O distance (l_{o-o}) of cation-GO complexes with the three of oxygen atoms, O_1 - O_3

The r_{O1-O3} represents the distance measured from the projection of the divalent transition metal cation on O_1 - O_2 - O_3 plane to the oxygen atoms at adsorption sites (Figure 4.13 (a)). The bond distance (l_{O1-O2}) was measured from the oxygen-oxygen atom of functional groups on O_1 - O_2 - O_3 plane (Figure 4.13 (b)).

From Table 4.4 and Figure 4.14, we found evidence to suggest that Cu^{2+} mainly localized on the position 2 (between hydroxyl and epoxy group) but another cations mainly localized on the same position 3 (between two epoxy groups). The influences of the divalent transition metal cations to the functional groups were investigated with the distance (l_{O1-O2} , l_{O2-O3} , l_{O1-O3}) between oxygen atoms of positions. To determine stable structures, we have many parameters to consider the influences of the divalent transition metal cations.

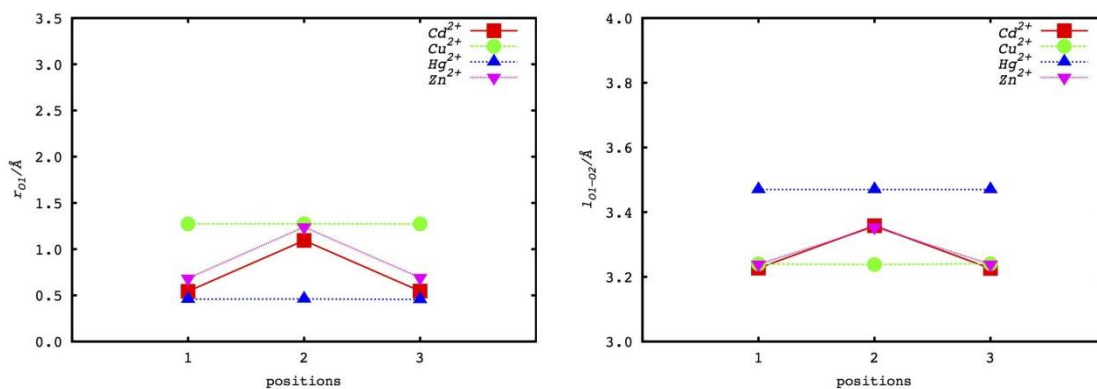


Figure 4. 14: The distance (r_{O1}), and O-O distance (l_{O1-O2}) of M^{2+} -GO complexes with 3 positions at B3LYP/6-31g(d).

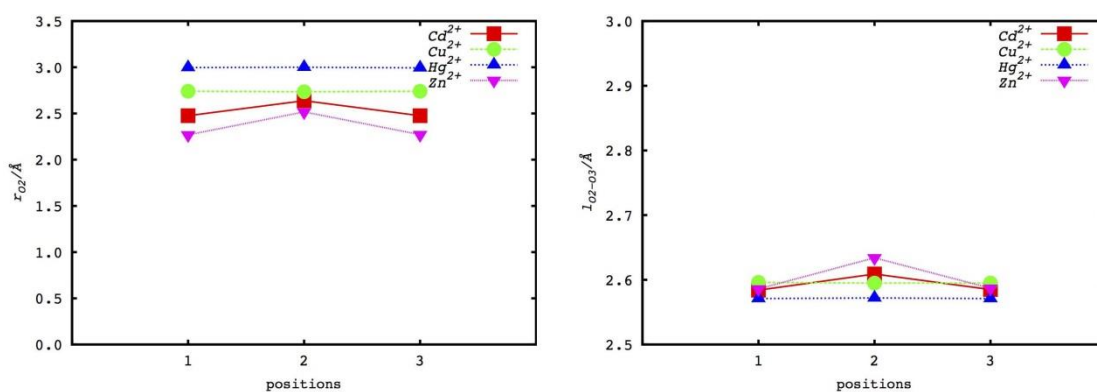


Figure 4. 15: The distance (r_{O2}), and O-O distance (l_{O2-O3}) of M^{2+} -GO complexes with 3 positions at B3LYP/6-31g(d).

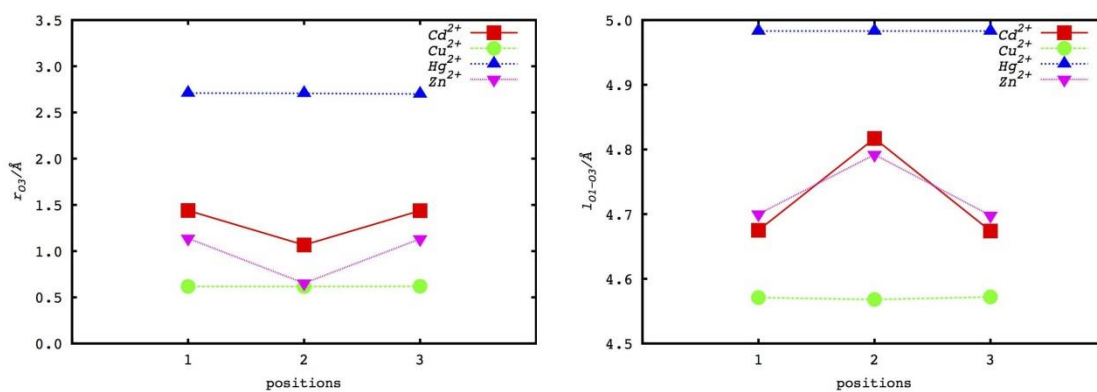


Figure 4. 16: The distance (r_{O3}) and O-O distance (l_{O1-O3}) of M^{2+} -GO complexes with 3 positions at B3LYP/6-31g(d).

The configurations with epoxy pair and hydroxyl groups on the GO complexes have been considered in a term of O-O distance (l_{o-o}). For the behavior of divalent metals, we consider the Cd^{2+} , Cu^{2+} , Hg^{2+} and Zn^{2+} . In this current study, we focus on the positions of divalent metal cations on GO surface before and after adsorption process. We limited the number of functional groups on the GO surface but keep C/O ratio constant like a Lerf-Klinowski model [63].

Now, we turn to focus the divalent metal cations adsorbed on GO surface. We found that the Cu^{2+} and Hg^{2+} cations like to move to position 2 when the starting points were 1, 2 and 3. Figure 4.14, 4.15 and 4.16 shows O-O distance (l_{o-o}) as positions of metal. The analysis of O-O distance (l_{o-o}) showed that the coordinate of both metals comes mostly constant position, because O-O distance (l_{o-o}) kept constant value for all positions. It is evident that Cu^{2+} and Hg^{2+} cations did not move to another position. The results seem to indicate that this causes the behavior to become extremely interaction with lone pair electrons of functional groups on GO surface.

However, in case of Cd^{2+} - and Zn^{2+} - complexes, the small fluctuate position was observed. The O-O distance (l_{o-o}) showed that the coordinate of both metals did not constant especially at position 2. Due to, both cations have been fluctuate interact between the hydroxyl and epoxy functional groups.

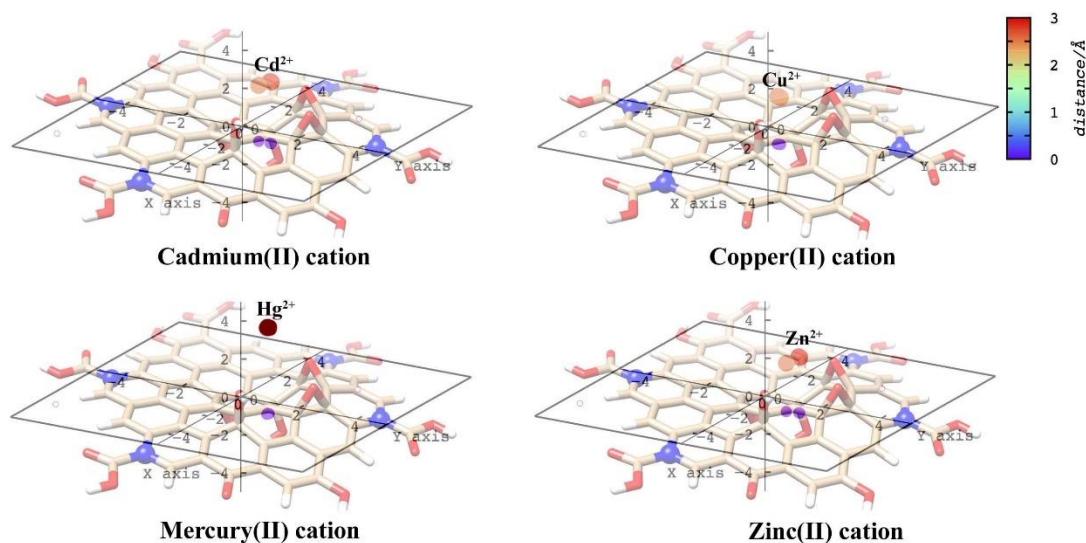


Figure 4. 17: The projection of divalent metal cations on xy -plane of GO. Distance of cations to xy -plane [\AA] was shaded by colour.

Figure 4.17 illustrates the findings of the position of divalent metal cations on the GO surface. The purple color in the 3D plot indicated the x , y coordinate on xy -plane of GO surface. As shown in Figure 4.17, the coordinate of divalent metal cations, especially for Cu^{2+} and Hg^{2+} cations have a single point on xy -plane. This suggests that both metals adsorption on GO surface are mainly localized on the same position for each metal cation. For the Cd^{2+} and Zn^{2+} cations, the coordinate of divalent metal cations have two point positions on xy -plane.

4.2.5 Effect of metal cation with curvature of GO complex

To investigate the effect of the curvature (complex geometry) on the divalent metal interaction, characteristic distances for the Cd^{2+} , Cu^{2+} , Hg^{2+} and Zn^{2+} cations complexes were summarized in Figure 4.19 and Table 4.4. From the geometry of the initial state, the form complex and equilibrium shapes at metal-GO complex are measured. The central points have the ability to move vertically upward. Additionally,

the radius of the metal cation can be estimated from the curvature of the GO plane. The curvature distances (h) were measured from complex form on the top (h_1) and bottom (h_2) of surface to the plane of the GO surface (see in Figure 4.18). In this way, we can study the influence of metal cation with the curvature of GO complexes by the difference of h_1 and h_2 with and without metal cations.

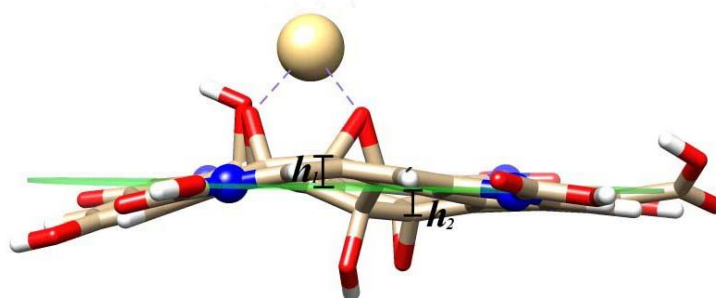


Figure 4. 18: The curvature ($h_{1,2}$) of GO complexes

Figure 4.19 and Table 4.4 show the characteristics of all GO complexes investigated in this work. The curvatures of GO complexes were constant for all positions. The results were investigated separately for two types of the complexes, where the cations are located on top or bottom of the GO sheet. The size of metal cations evaluated here are relatively. In this case, the h_1 can represent the influence of the divalent metal cations on the geometry of GO. The different metal cations on the GO surface can cause different distortions. In Figure 4.19, the curvature distortions of the GO complexes are influenced by the adsorption of the metal cations. It can be seen that the distortion of the curvature (Δh_1-h_2) of Hg^{2+} was higher than for all the other cations being 0.847 Å. These distortion patterns were induced by the ionic radius of metals.

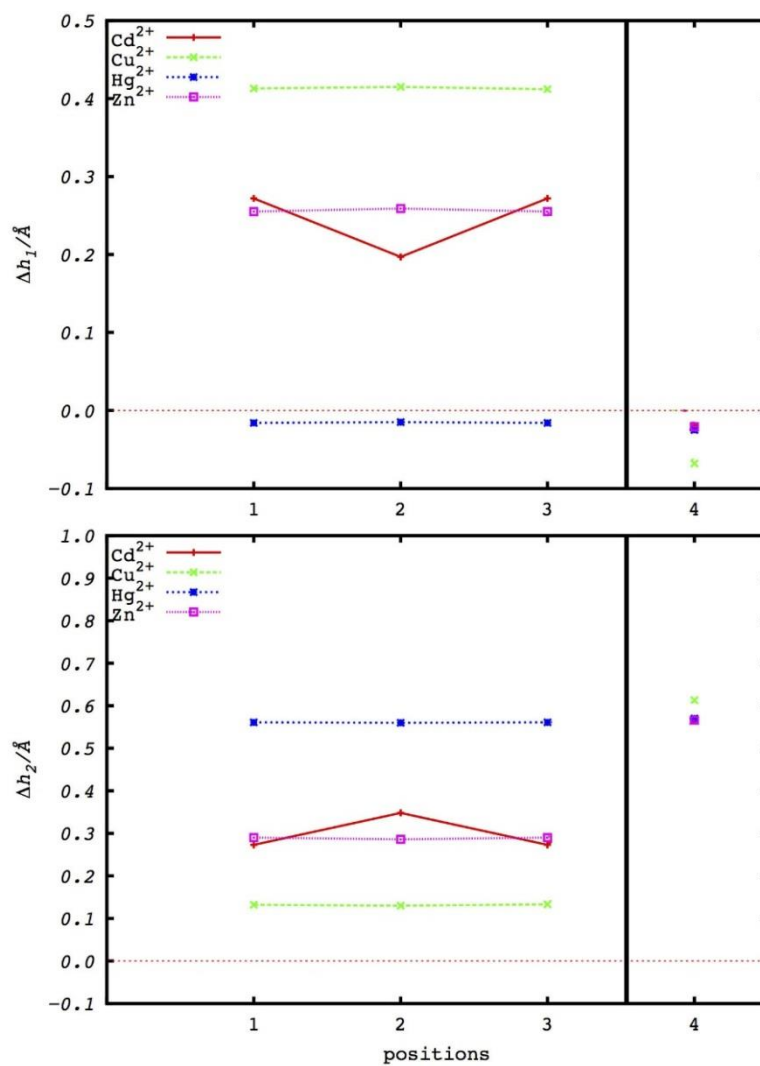


Figure 4. 19: The curvature ($\Delta h_{1,2}$) of GO complexes four divalent metals with 4 positions at B3LYP/6-31g(d).

4.2.6 Adsorption of Cu^{2+} cation on GO sheet

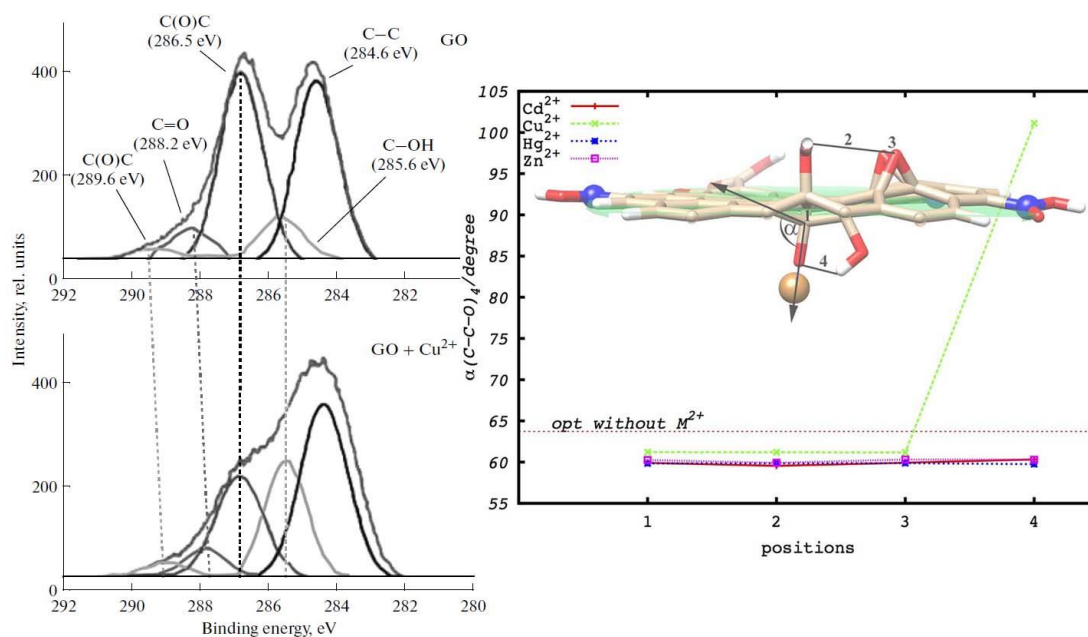


Figure 4. 20: (left) X-ray photoelectron spectra (C1s) of GO and GO+Cu²⁺ from ref [95] and (right) the angle α relate to divalent cation adsorption

The X-ray photoelectron spectra (XPS) of the initial GO and the GO complexes are shown in Figure 4.20. The spectrum of the epoxy C-O-C group on the GO surface is 286.5 eV. The differences include a reduced twice time intensity of the peak due to epoxy group broken by the Cu²⁺ cation. It is evident that the epoxy group can also convert to hydroxyl group. This result can confirm by quantum calculation. The picture insert shown that the functional groups of GO have been destroy by the Cu²⁺ metal cation. Figure 4.20 right hand side, illustrates the angle (α) is defined by the angle between C-C-O of epoxide group on bottom of GO. From this result, the angle (α) of Cu²⁺-GO complex was changed from about 60° to 110°. These results demonstrate that improved correlations with the experimental results are in good agreement with ref. [96]. These findings can be applied effectively utilized for the treatment of industrial waste by GO.

CHAPTER V

CONCLUSION

The electronic properties of single-walled carbon nanotubes (SWCNTs) can be modified by deforming their structures under high pressure. The aim of this study was to investigate the molecular structures and energy band gap of armchair and zigzag SWCNTs with various sizes and deformed shapes. To model the pressure effect, the degree of flatness (η) of the SWCNT was adjusted as the primary parameter. The results gave the C-C bond lengths and C-C-C bond angles of SWCNTs in the distorted states, and the structure distortion significantly affected the electronic property in term of different energy band gap. With increased η values in all studied SWCNTs, the bond lengths at the flattened region on where η applied were dramatically lengthened, while those at tube edge region were slightly decreased. This leads to the wider and narrower angles at the flattened and edge regions, consequently. Although the trend of the bond length and the angle changes were in the same pattern in the five different sizes of zigzag and armchair distorted tubes, less curvature effect on the angles at the edge region was only found in the zigzag tubes. As a function of the mechanical deformation, an electronic band gap is reduced leading to a semiconductor-metal transition for the (10,0), (20,0) and (25,0) zigzag SWCNTs and in vice versa for (15,0) SWCNT. Differentially, the metal-semiconductor transition is found in the armchair tube under applied low η value of 0.1 and followed by a reverse transition at the high η values. These results may contribute to a more refined design of new nano-electronic devices.

We performed a systematic DFT investigation of the adsorption of Cd^{2+} , Cu^{2+} , Hg^{2+} and Zn^{2+} on GO surface. The interactions between the divalent metal ions and the GO have been determined. The positions 1-3 were at the top of GO sheet, while the position 4 was at the bottom of GO sheet. Position 1 was placed at the GO center without any functional group. Position 2 was at between the epoxide and hydroxyl groups. The position 3 was located between the two epoxide groups. Lastly, the position 4 was opposite to position 1 at the bottom of GO sheet with nearby epoxide and hydroxyl groups. Geometries and energies of adsorption demonstrate the interaction of divalent metal with the functional groups on the GO surface. The binding efficiency of these divalent metals to GO surface increased in the following order: $\text{Cu}^{2+} > \text{Hg}^{2+} > \text{Zn}^{2+} > \text{Cd}^{2+}$. The binding energies of Cu^{2+} are much lower than those of Hg^{2+} , Cd^{2+} and Zn^{2+} , and the corresponding binding distances are much shorter. It is clear that the bonding in such systems is quite different from the effect we are discussing here because of interactions with d orbitals on the metal. Considering that the epoxy and hydroxyl groups are the main active oxide groups of GO for the adsorptions process, and epoxy group can also convert to hydroxyl group by the Cu^{2+} . It is evidence for presented. This is the first calculations evidence for the structures of GO-metal complexes. The Cu^{2+} cation has strongest interaction with the hydroxyl and epoxy functional groups. While, the two epoxy groups are the main active oxide groups of GO for the adsorption of the other cations. The epoxy group may convert to hydroxyl group by the Cu^{2+} adsorption. However, further experiments and higher level calculations are necessary to definitively elucidate these structures. Understanding the behavior by which divalent metal cations adsorb on the GO surface it would be useful

to design effective control technologies of the heavy metal pollution in industrial.
Future work should therefore consider the effect of aqueous solution.



REFERENCES

1. Iijima, S., *Helical microtubes of graphitic carbon*. Nature, 1991. **354**(Nov. 7): p. 56-58.
2. Saito, R., G. Dresselhaus, and M.S. Dresselhaus, *Physical Properties of Carbon Nanotube*. 1998: Imperial College Press.
3. Avramov, P.V., K.N. Kudin, and G.E. Scuseria, *Single wall carbon nanotubes density of states: comparison of experiment and theory*. Chemical Physics Letters, 2003. **370**(5-6): p. 597-601.
4. Dresselhaus, M.S., et al., *Raman spectroscopy of carbon nanotubes*. Physics Reports, 2005. **409**(2): p. 47-99.
5. Kim, C., et al., *Electronic structures of capped carbon nanotubes under electric fields*. Physical Review B, 2002. **65**(16): p. 165418-165423.
6. McEuen, P.L., et al., *Disorder, Pseudospins, and Backscattering in Carbon Nanotubes*. Physical Review Letters, 1999. **83**(24): p. 5098-5101.
7. Poklonski, N.A., et al., *Uniaxially deformed (5,5) carbon nanotube: Structural transitions*. Chemical Physics Letters, 2008. **464**(4-6): p. 187-191.
8. Qian, D., et al., *Mechanics of carbon nanotubes*. Applied Mechanics Reviews, 2002. **55**(6): p. 495-533.
9. Wongkoblap, A., et al., *Characterization of Single Wall Carbon Nanotubes and Activated Carbon with Water Adsorption in Finite-Length Pore Models*. Engineering Journal, 2013. **17**(4): p. 93-109.
10. Wilder, J.W.G., et al., *Electronic structure of atomically resolved carbon nanotubes*. Nature, 1998. **391**(6662): p. 59-62.
11. Frank, S., et al., *Carbon Nanotube Quantum Resistors*. Science, 1998. **280**(5370): p. 1744-1746.
12. Hone, J., M. Whitney, and A. Zettl, *Thermal conductivity of single-walled carbon nanotubes*. Synthetic Metals, 1999. **103**(1-3): p. 2498-2499.
13. Yu, M.-F., et al., *Tensile Loading of Ropes of Single Wall Carbon Nanotubes and their Mechanical Properties*. Physical Review Letters, 2000. **84**(24): p. 5552-5555.
14. Jindal, V.K. and A.N. Imtani, *Bond lengths of armchair single-walled carbon nanotubes and their pressure dependence*. Computational Materials Science, 2008. **44**(1): p. 156-162.

15. Rochefort, A., D.R. Salahub, and P. Avouris, *The effect of structural distortions on the electronic structure of carbon nanotubes*. Chemical Physics Letters, 1998. **297**(1–2): p. 45-50.
16. Umeno, Y., T. Kitamura, and A. Kushima, *Theoretical analysis on electronic properties of zigzag-type single-walled carbon nanotubes under radial deformation*. Computational Materials Science, 2004. **30**(3-4): p. 283-287.
17. Wang, B., et al., *Effect of bending on single-walled carbon nanotubes: A Raman scattering study*. Physical Review B, 2010. **81**(11): p. 115422-115427.
18. Yang, X.-p., G. Wu, and J.-m. Dong, *Structural and vibrational properties of deformed carbon nanotubes*. Frontiers of Physics in China, 2009. **4**(3): p. 280-296.
19. Gülseren, O., T. Yildirim, and S. Ciraci, *Systematic ab initio study of curvature effects in carbon nanotubes*. Physical Review B, 2002. **65**(15): p. 153405-153408.
20. Imtani, A.N. and V.K. Jindal, *Structure of armchair single-wall carbon nanotubes under hydrostatic pressure*. Physical Review B, 2007. **76**(19): p. 195447-195455.
21. Imtani, A.N. and V.K. Jindal, *Pressure effects on bond lengths and shape of zigzag single-walled carbon nanotubes*. Computational Materials Science, 2009. **44**(4): p. 1142-1149.
22. Qing, Q., et al., *Local Gate Effect of Mechanically Deformed Crossed Carbon Nanotube Junction*. Nano Letters, 2010. **10**(11): p. 4715-4720.
23. Falvo, M.R., et al., *Bending and buckling of carbon nanotubes under large strain*. Nature, 1997. **389**(6651): p. 582-584.
24. Bezryadin, A., et al., *Multiprobe Transport Experiments on Individual Single-Wall Carbon Nanotubes*. Physical Review Letters, 1998. **80**(18): p. 4036-4039.
25. Chopra, N.G., et al., *Fully collapsed carbon nanotubes*. Nature, 1995. **377**(6545): p. 135-138.
26. Yang, X., et al., *Single-walled carbon nanotube bundle under hydrostatic pressure studied by first-principles calculations*. Physical Review B, 2006. **73**(23): p. 235403-235408.
27. Tang, J., et al., *Revealing properties of single-walled carbon nanotubes under high pressure*. Journal of Physics-Condensed Matter, 2002. **14**(44): p. 10575-10578.
28. Gadagkar, V., et al., *Collapse of double-walled carbon nanotube bundles under hydrostatic pressure*. Physical Review B, 2006. **73**(8): p. 085402-085407.

29. Shan, G. and S. Bao, *The effect of deformations on electronic structures and optical properties of carbon nanotubes*. Physica E: Low-dimensional Systems and Nanostructures, 2006. **35**(1): p. 161-167.
30. Peters, M.J., et al., *Structural phase transition in carbon nanotube bundles under pressure*. Physical Review B, 2000. **61**(9): p. 5939-5944.
31. Liu, B., et al., *The influence of mechanical deformation on the electrical properties of single wall carbon nanotubes*. Journal of the Mechanics and Physics of Solids, 2004. **52**(1): p. 1-26.
32. Nishidate, K. and M. Hasegawa, *Universal band gap modulation by radial deformation in semiconductor single-walled carbon nanotubes*. Physical Review B, 2008. **78**(19).
33. Rochefort, A., D.R. Salahub, and P. Avouris, *The effect of structural distortions on the electronic structure of carbon nanotubes*. Chemical Physics Letters, 1998. **297**(1-2): p. 45-50.
34. Caillier, C., et al., *Probing high-pressure properties of single-wall carbon nanotubes through fullerene encapsulation*. Physical Review B, 2008. **77**(12): p. 125418-125426.
35. Lu, S., et al., *Exploring the possible interlinked structures in single-wall carbon nanotubes under pressure by Raman spectroscopy*. Journal of Raman Spectroscopy, 2013. **44**(2): p. 176-182.
36. Avramov, P.V., K.N. Kudin, and G.E. Scuseria, *Single wall carbon nanotubes density of states: comparison of experiment and theory*. Chemical Physics Letters, 2003. **370**(5-6): p. 597-601.
37. Mazzoni, M.S.C. and H. Chacham, *Bandgap closure of a flattened semiconductor carbon nanotube: A first-principles study*. Applied Physics Letters, 2000. **76**(12): p. 1561-1563.
38. Shan, B., et al., *First-principles study of band-gap change in deformed nanotubes*. Applied Physics Letters, 2005. **87**(17): p. 173109-3.
39. Park, S. and R.S. Ruoff, *Chemical methods for the production of graphenes*. Nat Nanotechnol, 2009. **4**(4): p. 217-24.
40. Novoselov, K.S., et al., *Electric Field Effect in Atomically Thin Carbon Films*. Science, 2004. **306**(5696): p. 666-669.
41. Hummers, W.S. and R.E. Offeman, *Preparation of Graphitic Oxide*. Journal of the American Chemical Society, 1958. **80**(6): p. 1339-1339.

42. Lu, S.C., et al., *Exploring the possible interlinked structures in single-wall carbon nanotubes under pressure by Raman spectroscopy*. Journal of Raman Spectroscopy, 2013. **44**(2): p. 176-182.
43. Acik, M., et al., *Unusual infrared-absorption mechanism in thermally reduced graphene oxide*. Nat Mater, 2010. **9**(10): p. 840-845.
44. Bohr, N., *I. On the constitution of atoms and molecules*. Philosophical Magazine Series 6, 1913. **26**(151): p. 1-25.
45. Planck, M., *Ueber das Gesetz der Energieverteilung im Normalspectrum*. Annalen der Physik, 1901. **309**(3): p. 553-563.
46. Broglie, L.d., *Recherches sur la théorie des quanta*. Ann. de Physique, 1925. **10**(3): p. 22-128.
47. Davisson, C. and L.H. Germer, *Diffraction of Electrons by a Crystal of Nickel*. Physical Review, 1927. **30**(6): p. 705-740.
48. Schrödinger, E., *Quantisierung als Eigenwertproblem*. Annalen der Physik, 1926. **384**(4): p. 361-376.
49. Kohn, W. and L.J. Sham, *Self-Consistent Equations Including Exchange and Correlation Effects*. Physical Review, 1965. **140**(4A): p. A1133-A1138.
50. Perdew, J.P., K. Burke, and M. Ernzerhof, *Generalized Gradient Approximation Made Simple*. Physical Review Letters, 1996. **77**(18): p. 3865-3868.
51. Becke, A.D., *Density-functional exchange-energy approximation with correct asymptotic behavior*. Physical Review A, 1988. **38**(6): p. 3098-3100.
52. Gill, P.M.W., et al., *The performance of the Becke—Lee—Yang—Parr (B—LYP) density functional theory with various basis sets*. Chemical Physics Letters, 1992. **197**(4–5): p. 499-505.
53. Lee, C., W. Yang, and R.G. Parr, *Development of the Colle-Salvetti correlation-energy formula into a functional of the electron density*. Physical Review B, 1988. **37**(2): p. 785-789.
54. Perdew, J.P., *Density-functional approximation for the correlation energy of the inhomogeneous electron gas*. Physical Review B, 1986. **33**(12): p. 8822-8824.
55. Perdew, J.P., et al., *Atoms, molecules, solids, and surfaces: Applications of the generalized gradient approximation for exchange and correlation*. Physical Review B, 1992. **46**(11): p. 6671-6687.
56. Vosko, S.H., L. Wilk, and M. Nusair, *Accurate spin-dependent electron liquid correlation energies for local spin density calculations: a critical analysis*. Canadian Journal of Physics, 1980. **58**(8): p. 1200-1211.

57. Zhao, Y. and D. Truhlar, *The M06 suite of density functionals for main group thermochemistry, thermochemical kinetics, noncovalent interactions, excited states, and transition elements: two new functionals and systematic testing of four M06-class functionals and 12 other functionals*. Theoretical Chemistry Accounts, 2008. **120**(1-3): p. 215-241.
58. Fuchs, M. and M. Scheffler, *Ab initio pseudopotentials for electronic structure calculations of poly-atomic systems using density-functional theory*. Computer Physics Communications, 1999. **119**(1): p. 67-98.
59. Orlando, R., et al., *Ab initio Hartree-Fock calculations for periodic compounds: application to semiconductors*. Journal of Physics: Condensed Matter, 1990. **2**(38): p. 7769-7789.
60. Inc, A.S., *Material Studio Modeling Environment*. 2007, Release 5.5 San Diego.
61. Milman, V., et al., *Electron and vibrational spectroscopies using DFT, plane waves and pseudopotentials: CASTEP implementation*. Journal of Molecular Structure-Theochem, 2010. **954**(1-3): p. 22-35.
62. Monkhorst, H.J. and J.D. Pack, *Special points for Brillouin-zone integrations*. Physical Review B, 1976. **13**(12): p. 5188-5192.
63. He, H., et al., *A new structural model for graphite oxide*. Chemical Physics Letters, 1998. **287**(1-2): p. 53-56.
64. Dreyer, D.R., et al., *The chemistry of graphene oxide*. Chemical Society Reviews, 2010. **39**(1): p. 228-240.
65. Casabianca, L.B., et al., *NMR-Based Structural Modeling of Graphite Oxide Using Multidimensional ¹³C Solid-State NMR and ab Initio Chemical Shift Calculations*. Journal of the American Chemical Society, 2010. **132**(16): p. 5672-5676.
66. Rungnim, C., *Theoretical study on the use of carbon nanotube as carrier for targeted drug delivery system*, in Graduate school. 2012, Chulalongkorn University. p. 81.
67. Antony, J. and S. Grimme, *Structures and interaction energies of stacked graphene-nucleobase complexes*. Physical Chemistry Chemical Physics, 2008. **10**(19): p. 2722-2729.
68. Yang, Y., M.N. Weaver, and K.M. Merz, *Assessment of the "6-31+G** + LANL2DZ" Mixed Basis Set Coupled with Density Functional Theory Methods and the Effective Core Potential: Prediction of Heats of Formation and Ionization Potentials for First-Row-Transition-Metal Complexes*. The Journal of Physical Chemistry A, 2009. **113**(36): p. 9843-9851.

69. Martin, J.M.L. and A. Sundermann, *Correlation consistent valence basis sets for use with the Stuttgart-Dresden-Bonn relativistic effective core potentials: The atoms Ga-Kr and In-Xe*. Journal of Chemical Physics, 2001. **114**(8): p. 3408-3420.
70. Boys, S.F. and F. Bernardi, *The calculation of small molecular interactions by the differences of separate total energies. Some procedures with reduced errors*. Molecular Physics, 1970. **19**(4): p. 553-566.
71. Frisch, M.J., et al., *Gaussian 09, Revision B.01*. 2009: Wallingford CT.
72. Ouyang, M., et al., *Energy gaps in "metallic" single-walled carbon nanotubes*. Science, 2001. **292**(5517): p. 702-5.
73. Reich, S., C. Thomsen, and P. Ordejón, *Elastic properties of carbon nanotubes under hydrostatic pressure*. Physical Review B, 2002. **65**(15): p. 153407-153410.
74. Reich, S., C. Thomsen, and P. Ordejon, *Electronic band structure of isolated and bundled carbon nanotubes*. Physical Review B, 2002. **65**(15): p. 155411-155421.
75. Ito, T., et al., *First principles calculations for electronic band structure of single-walled carbon nanotube under uniaxial strain*. Surface Science, 2002. **514**(1-3): p. 222-226.
76. Matsuda, Y., J. Tahir-Kheli, and W.A. Goddard, *Definitive Band Gaps for Single-Wall Carbon Nanotubes*. The Journal of Physical Chemistry Letters, 2010. **1**(19): p. 2946-2950.
77. Gülseren, O., et al., *Reversible band-gap engineering in carbon nanotubes by radial deformation*. Physical Review B, 2002. **65**(15): p. 155410-155416.
78. Yildirim, T., O. Gulseren, and S. Ciraci, *Exohydrogenated single-wall carbon nanotubes*. Physical Review B, 2001. **64**(7): p. 075404-075408.
79. Akai, Y. and S. Saito, *Electronic structure, energetics and geometric structure of carbon nanotubes: A density-functional study*. Physica E: Low-dimensional Systems and Nanostructures, 2005. **29**(3-4): p. 555-559.
80. Rochefort, A., D.R. Salahub, and P. Avouris, *Effects of Finite Length on the Electronic Structure of Carbon Nanotubes*. The Journal of Physical Chemistry B, 1999. **103**(4): p. 641-646.
81. Pullen, A., et al., *Structural, elastic, and electronic properties of deformed carbon nanotubes under uniaxial strain*. Physical Review B, 2005. **71**(20): p. 205410-205414.
82. Motavas, S., A. Ivanov, and A. Nojeh, *The curvature of the nanotube sidewall and its effect on the electronic and optical properties of zigzag nanotubes*. Computational and Theoretical Chemistry, 2013. **1020**(0): p. 32-37.

83. Rubio, A., *Spectroscopic properties and STM images of carbon nanotubes*. Applied Physics a-Materials Science & Processing, 1999. **68**(3): p. 275-282.
84. Tomblor, T.W., et al., *Reversible electromechanical characteristics of carbon nanotubes under local-probe manipulation*. Nature, 2000. **405**(6788): p. 769-772.
85. Blase, X., et al., *Hybridization effects and metallicity in small radius carbon nanotubes*. Physical Review Letters, 1994. **72**(12): p. 1878-1881.
86. Steckel, J.A., *Ab initio modelling of neutral and cationic Hg-benzene complexes*. Chemical Physics Letters, 2005. **409**(4-6): p. 322-330.
87. Ho, Y.-P., et al., *Binding Energies of Ag⁺ and Cd⁺ Complexes from Analysis of Radiative Association Kinetics*. The Journal of Physical Chemistry A, 1997. **101**(18): p. 3338-3347.
88. Meyer, F., F.A. Khan, and P.B. Armentrout, *Thermochemistry of Transition Metal Benzene Complexes: Binding Energies of M(C₆H₆)_x⁺ (x = 1, 2) for M = Ti to Cu*. Journal of the American Chemical Society, 1995. **117**(38): p. 9740-9748.
89. Chen, Y.-M. and P.B. Armentrout, *Collision-induced dissociation of Ag (C₆H₆)⁺*. Chemical Physics Letters, 1993. **210**(1-3): p. 123-128.
90. Leszczynski, J., *Computational Chemistry: Reviews of Current Trends*. Vol. 10. 2006: World Scientific Publishing Company, Incorporated.
91. Brandenburg, J.G., et al., *Geometrical Correction for the Inter- and Intramolecular Basis Set Superposition Error in Periodic Density Functional Theory Calculations*. The Journal of Physical Chemistry A, 2013. **117**(38): p. 9282-9292.
92. Ogata, C., et al., *Metal Permeation into Multi-layered Graphene Oxide*. Scientific Reports, 2014. **4**: p. 1-6.
93. Bauschlicher, C.W., H. Partridge, and S.R. Langhoff, *Theoretical study of transition-metal ions bound to benzene*. The Journal of Physical Chemistry, 1992. **96**(8): p. 3273-3278.
94. Ozutsumi, K., et al., *Solvation structure of divalent transition-metal ions in N,N-dimethylformamide and N,N-dimethylacetamide*. The Journal of Physical Chemistry, 1993. **97**(2): p. 500-502.
95. Laure, I.L., et al., *The coordination chemistry of graphene oxide: Interactions with metal ions in water*. Russian Journal of Coordination Chemistry, 2013. **39**(7): p. 487-492.

96. Hu, C.G., et al., *Spontaneous Reduction and Assembly of Graphene oxide into Three-Dimensional Graphene Network on Arbitrary Conductive Substrates*. Scientific Reports, 2013. **3**: p. 1-10.





APPENDIX

จุฬาลงกรณ์มหาวิทยาลัย
CHULALONGKORN UNIVERSITY

VITA

Biography

Name: Mr. Somphob Thompho

Date of Birth: 4 March 1976

Place of Birth: Nakhon Ratchasima, Thailand

Education

1982 - 1987 Primary school 'Muang Nakhon Rachasima School'

Nakhon Rachasima

1988 - 1990 Secondary school 'Rajsima Witthayalai School'

Nakhon Rachasima

1991 - 1993 High school 'Rajsima Witthayalai School', Nakhon Rachasima

1994 - 1997 B. Sc. in Chemistry at Khon Kaen University, Khon Kaen

1998 - 2001 M. Sc. in Physical Chemistry at Khon Kaen University,
Khon Kaen, thesis: 'A Theoretical Study of the Hydration of Silver (I) Ion on
Coronene'

since 2004 Ph. D. study at the Department of Chemistry,
Chulalongkorn University, Bangkok